Numerical and Experimental Studies of Wakefield Accelerators

Ekerfelt, Henrik

2019

Document Version:
Publisher's PDF, also known as Version of record

Numerical and Experimental Studies of Wakefield Accelerators

HENRIK EKERFELT

DOCTORAL THESIS

Faculty of Engineering, LTH
Department of Physics
Division of Atomic Physics
Lund University

Numerical and Experimental Studies of Wakefield Accelerators

Henrik Ekerfelt

LUND
UNIVERSITY

Akademisk avhandling som för avläggande av teknologie doktorsexamen vid tekniska fakulteten vid Lunds universitet kommer att offentligen försvaras den 14 juni 2019, kl. 13.15 i Rydbergssalen, på Fysiska institutionen, Professorsgatan 1, Lund.
Fakultetsopponent: Jens Osterhoff
Deutsches Elektronen-Synchrotron DESY, Hamburg, Tyskland

Academic dissertation which, by due permission of the Faculty of Engineering at Lund University, will be publicly defended on June 14, 2019, at 13.15 a.m. in the Rydberg hall, at the Department of Physics, Professorsgatan 1, Lund, for the degree of Doctor of Philosophy in Engineering.
Faculty opponent: Jens Osterhoff
Deutsches Elektronen-Synchrotron DESY, Hamburg, Germany

Organization
LUND UNIVERSITY

Atomic Physics
Department of Physics
P.O. Box 118
SE-112 00 Lund
Sweden

Document name
DOCTORAL DISSERTATION

Date of disputation
14th June 2019

Sponsoring organization

Author(s)
Henrik Ekerfelt

Title and subtitle
Numerical and Experimental Studies of Wakefield Accelerators

Abstract
This thesis is based on work done by the author on the development of laser wakefield accelerators. Wakefield acceleration in plasmas is a promising technique to provide the next generation of accelerating structures and particle beams. Plasmas can sustain electric fields that are many orders of magnitude stronger than those possible in conventional accelerators. Other benefits of wakefield accelerators are that electron beams produced inside the plasma can be generated with high peak current and ultra-low emittance. These strongly accelerating structures can reduce the size of particle accelerators, making them more available, for example in hospitals, or to increase the energy in particle colliders. In wakefield acceleration, a driver is used to excite a plasma wave. The acceleration of charged particles takes place in a plasma wave excited by, and co-propagating with, the driver. The driver can be a laser pulse or a bunch of charged particles. However, many technical challenges remain to be solved before a reliable particle source can be realized based on this technology.

This thesis describes numerical studies performed using particle-in-cell simulations and experimental work using high-intensity laser pulses, with the aim of improving our knowledge on wakefield accelerators. The work presented here focuses on three different topics: trapping mechanisms, achieving higher electron energies and improvement of the betatron X-rays generated. In particular, trapping in a density down-ramp, ionization induced trapping, and trapping by colliding pulses have been investigated numerically and experimentally. A novel guidance technique for high-intensity laser pulses is suggested, the merging of two laser wakefields is experimentally demonstrated and suggested as a possible means of staging wakefield accelerators, and the possibility of carrying out a beam-driven plasma wakefield experiment is investigated through simulations. An improved X-ray source based on laser wakefield acceleration and enhancement of the betatron oscillations through direct laser acceleration is investigated and two applications are demonstrated.

Key words
Laser-wakefield acceleration, betatron radiation, ionization-induced trapping, density down-ramp trapping, colliding pulse injection, direct laser acceleration, laser-wakefield merging, particle-in-cell simulations, high-intensity optics

Classification system and/or index terms (if any)

Supplementary bibliographical information

Language
English

ISSN and key title

ISBN
978-91-7895-127-7(print)
978-91-7895-128-4(pdf)

Recipient's notes

Number of pages
166

Price

Security classification

Signature 

Date 8 May 2019

Numerical and Experimental Studies of Wakefield Accelerators

Henrik Ekerfelt

Doctoral Thesis
2019

Lund University

Numerical and Experimental Studies of
Wakefield Accelerators

Printed in Sweden by Media-Tryck, Lund, 2019

Division of Atomic Physics
Department of Physics
Faculty of Engineering, LTH
Lund University
P.O. Box 118
SE-221 00 Lund
Sweden
www.atomic.physics.lu.se

ISSN 0281-2762
Lund Reports on Atomic Physics, LRAP 559 (2019)
ISBN 978-91-7895-127-7 (print)
ISBN 978-91-7895-128-4 (pdf)

Abstract

This thesis is based on work done by the author on the development of laser wakefield accelerators. Wakefield acceleration in plasmas is a promising technique to provide the next generation of accelerating structures and particle beams. Plasmas can sustain electric fields that are many orders of magnitude stronger than those possible in conventional accelerators. Other benefits of wakefield accelerators are that electron beams produced inside the plasma can be generated with high peak current and ultra-low emittance. These strongly accelerating structures can reduce the size of particle accelerators, making them more available, for example in hospitals, or to increase the energy in particle colliders. In wakefield acceleration, a driver is used to excite a plasma wave. The acceleration of charged particles takes place in a plasma wave excited by, and co-propagating with, the driver. The driver can be a laser pulse or a bunch of charged particles. However, many technical challenges remain to be solved before a reliable particle source can be realized based on this technology.

This thesis describes numerical studies performed using particle-in-cell simulations and experimental work using high-intensity laser pulses, with the aim of improving our knowledge on wakefield accelerators. The work presented here focuses on three different topics: trapping mechanisms, achieving higher electron energies and improvement of the betatron X-rays generated. In particular, trapping in a density down-ramp, ionization induced trapping, and trapping by colliding pulses have been investigated numerically and experimentally. A novel guidance technique for high-intensity laser pulses is suggested, the merging of two laser wakefields is experimentally demonstrated and suggested as a possible means of staging wakefield accelerators, and the possibility of carrying out a beam-driven plasma wakefield experiment is investigated through simulations. An improved X-ray source based on laser wakefield acceleration and enhancement of the betatron oscillations through direct laser acceleration is investigated and two applications are demonstrated.

Populärvetenskaplig sammanfattning

Vad händer när man låter korta starka ljuspulser färdas genom en gas? Om ljuset är starkt nog joniseras atomerna i gasen. En atom joniseras när en negativ elektron i atomen skiljs från den mycket tyngre positiva kärnan. När detta händer skapas ett så kallat plasma, där elektronerna och jonerna bildar en komplex vätska med laddade partiklar. Denna laddade vätska har många lustiga egenskaper som vi inte är vana vid att uppleva i vanlig materia, t.ex. kan det skapas starka elektromagnetiska vågor, som följer en densitetsändring i vätskan. Man kan också flytta på partiklarna i plasmat med ljus.

I sviterna av växelverkan mellan den korta starka laserpulsen och det plasma den bildat skapas en elektrondensitetsvåg, likt en kölvåg efter en båt på vattnet trycks elektronerna bort från laserpulsen när den passerar, för att sedan återvända och fylla tomrummet bakom laserpulsen. Den här elektrondensitetsvågen ger upphov till väldigt starka elektriska fält. Dessa fält följer laserpulsen och kan användas för att accelerera elektroner till nästan ljusets hastighet på väldigt korta sträckor. Man kan föreställa sig att de elektroner som accelereras surfar på den elektriska vågen likt en surfare på en vattenvåg. När elektronen surfar svänger den fram och tillbaka längs vågen, denna svängningsrörelse ger i sin tur upphov till en ny elektromagnetisk våg, i form av röntgen-strålning.

I den här avhandlingen har tre olika utmaningar för denna typ av elektronacceleration studerats. Den första handlar om hur man får elektronerna att börja surfa. I vårt plasma är det ju fullt av elektroner, men den stora majoriteten surfar inte. För att de ska lyckas surfa måste elektronen först färdas med vågen i en sådan hastighet att vågen inte bara passerar, utan så att elektronen innan vågen passerar uppnår nästan samma hastighet som vågen, likt en surfare som simmar i samma riktning som vågen innan hen ställer sig på surfbrädan. Det finns olika sätt att få detta att hända, i avhandlingen studeras tre olika tekniker för att få elektronerna att surfa.

Den andra utmaningen handlar om att få elektronerna att surfa så länge som möjligt. Här diskuteras ett antal olika metoder. Bland annat föreslås en lösning på hur man skulle kunna bygga en ljusguide för väldigt starka laserpulser, som fungerar som en kanal där ljuset kan färdas. Ett annat relaterat problem är att ljuspulsens energi tar slut. När ljuspulsen trycker på elektronerna tappar den energi, och till slut tar energin slut. Här gör vi ett experiment som visar hur vi skulle kunna föra in en ny stark ljuspuls som kan fortsätta skapa en plasmavåg.

Den sista utmaningen handlar om röntgenstrålning. Ett användningsområde för dessa surfande elektroner är som en röntgenkälla. Röntgenkällan blir starkare om elektronerna gör kraftigare svängningar. Framförallt undersöks hur svängningarna kan förstärkas när laserpulsen överlappar med de surfande elektronerna. Röntgenstrålarna som skapas kan användas för unika tillämpningar, bland annat visas hur de kan utnyttjas för att med tomografisk teknik göra en 3D-modell av en liten insekt. Slutligen visas hur ett instrument kan byggas för att studera vad som händer i material när de värms upp väldigt snabbt.

List of Publications

This thesis is based on eight papers which are appended at the end of the thesis, and referred to by their Roman numerals.

I **A tunable electron beam source using trapping of electrons in a density down-ramp in laser wakefield acceleration**
H. Ekerfelt, M. Hansson, I. Gallardo González, X. Davoine and O. Lundh.
Scientific Reports **7**, 12229 (2017).

II **Localization of ionization-induced trapping in a laser wakefield accelerator using a density down-ramp**
M. Hansson, T. L. Audet, H. Ekerfelt, B. Aurand, I. Gallardo González, F. G. Desforges, X. Davoine, A. Maitrallain, S. Reymond, P. Monot, A. Persson, S. Dobosz Dufrénoy, C.-G. Wahlström, B. Cros and O. Lundh.
Plasma Physics and Controlled Fusion **58**, 055009 (2016).

III **Injection of electrons by colliding laser pulses in a laser wakefield accelerator**
M. Hansson, B. Aurand, H. Ekerfelt, A. Persson, and O. Lundh.
Nuclear Instruments and Methods in Physics Research A **829**, 99 (2016).

IV **An acousto-optic waveguide for high-intensity lasers**
H. Ekerfelt, M. Hansson, and O. Lundh.
2019 Submitted manuscript.

V **Electron acceleration from merging laser wakefields**
I. Gallardo González, H. Ekerfelt, J. Björklund Svensson, G. Gatti, A. Gonoskov, D. Guénot, M. Hansson, M. Marklund, J. A. Pérez-Hernández, C. Salgado, E. Wallin, G. Zeraouli and O. Lundh.
2019 Manuscript in preparation.

VI **Effects of the dopant concentration in laser wakefield and direct laser acceleration of electrons**
I. Gallardo González, H. Ekerfelt, M. Hansson, T. L. Audet, B. Aurand, F. G. Desforges, S. Dobosz Dufrénoy, A. Persson, X. Davoine, C.-G. Wahlström, B. Cros and O. Lundh.
New Journal of Physics **20**, 053011 (2018).

VII **Highly efficient angularly resolving X-ray spectrometer optimized for absorption measurements with collimated sources**
M. Šmíd, I. Gallardo González, H. Ekerfelt, J. Björklund Svensson, M. Hansson, J. C. Wood, A. Persson, S. P. D. Mangles, O. Lundh and K. Falk.
Review of Scientific Instruments **88**, 063102 (2017).

VIII **Optimization of soft X-ray phase-contrast tomography using a laser wakefield accelerator**
K. Svendsen, I. Gallardo González, M. Hansson, J. Björklund Svensson, H. Ekerfelt, A. Persson and O. Lundh.
Optics Express **26**, 33930 (2018).

Other related publications by the author not included in this thesis:

Down-ramp injection and independently controlled acceleration of electrons in a tailored laser wakefield accelerator
M. Hansson, B. Aurand, X. Davoine, H. Ekerfelt, K. Svensson, A. Persson, C.-G. Wahlström, O. Lundh.
Physical Review Special Topics - Accelerators and Beams **20**, 071303 (2015).

Nano and micro structured targets to modulate the spatial profile of laser driven proton beams
L. Giuffrida, K. Svensson, J. Psikal, D. Margarone, P. Lutoslawski, V. Scuderi, G. Milluzzo, J. Kaufman, T. Wiste, M. Dalui, H. Ekerfelt, I. Gallardo González, O. Lundh, A. Persson, A. Picciotto, M. Crivellari, A. Bagolini, P. Bellutti, J. Magnusson, A. Gonoskov, L. Klimsa, J. Kopecek, T. Lastovicka, G.A.P. Cirrone, C.-G. Wahlström and G. Korn.
Journal of Instrumentation **12**, C03040 (2017).

Manipulation of laser-accelerated proton beam profiles by nanostructured and microstructured targets

L. Giuffrida, K. Svensson, J. Psikal, M. Dalui, H. Ekerfelt, I. Gallardo González, O. Lundh, A. Persson, P. Lutoslawski, V. Scuderi, J. Kaufman, T. Wiste, T. Lastovicka, A. Picciotto, A. Bagolini, M. Crivellari, P. Bellutti, G. Milluzzo, G. A. P. Cirrone, J. Magnusson, A. Gonoskov, G. Korn, C.-G. Wahlström and D. Margarone.

Physical Review Accelerators and Beams **20**, 081301 (2017).

Driver-Witness-Bunches for Plasma-Wakefield Acceleration at the MAX IV Linear Accelerator

J. Björklund Svensson, J. Andersson, F. Curbis, H. Ekerfelt, M. Kotur, F. Lindau, O. Lundh, E. Mansten, S. Thorin, S. Werin.

TUPIK031 (2017) *Proceedings, 8th International Particle Accelerator Conference (IPAC 2017): Copenhagen, Denmark, May 14-19, 2017.*

Beamline Design for Plasma-Wakefield Acceleration Experiments at MAX IV

J. Björklund Svensson, H. Ekerfelt, O. Lundh, E. Mansten, J. Andersson, M. Kotur, F. Lindau, S. Thorin, T.K. Charles.

1-4 (2018) *2018 IEEE Advanced Accelerator Concepts Workshop (AAC).*

Contents

Papers

Chapter 1

Introduction

The work presented in this thesis was dedicated to developing the technique employing plasma waves as an accelerating structure for electrons. The topic combines two powerful scientific instruments, namely lasers and particle accelerators. A high-intensity laser pulse can be used to excite a plasma wave, which in turn may be used to accelerate particles.

Particle accelerators play a vital role in society today. They can be found in medical applications, for example, as a source of ionizing radiation used to treat cancer or to obtain medical images for diagnostic purposes. Accelerators were originally developed as a tool to learn about nature and to expand the frontiers of the natural sciences. Particle accelerators have played a key role in physics in the development and confirmation of our most fundamental and complete theories about the laws governing our universe, the so-called Standard Model. However, high-energy particle accelerators are very large and expensive machines. The largest, and most powerful particle accelerator, called the Large Hadron Collider, has a circumference of 27 km and is located at CERN in a tunnel below Geneva in Switzerland. The accelerator technology used in this kind of accelerator has reached its limits. The only way to increase the energy significantly is to increase the size of the accelerator, making them prohibitively expensive. Therefore, the accelerator community is at, or close to, the end of the road regarding conventional technology in high-energy applications. One of the promising aspects of accelerating particles in plasma waves is that the accelerator could be made significantly smaller, and thus cheaper.

The concept of accelerating electrons in plasma waves was introduced in 1979 by Tajima and Dawson, working at the University of California, Los Angeles [1]. This was followed by experimental efforts to realize this kind of accelerator using different configurations. However, the lasers available at the time were not powerful enough to do this efficiently. As the technology developed, especially through the invention of chirped pulse amplification [2], quasi mono-energetic beams of electrons were produced by three different groups, and their results were published in Nature in 2004 [3–5]. This breakthrough sparked a massive increase in interest and activities in the research field.

Wakefield acceleration is a promising candidate for both a next-generation electron accelerators, and as a complement to next-generation X-ray sources. However, a num-

ber of problems must be solved before the technique can be transferred from research laboratories to applications in medicine, or other branches of physics or science. The work described in this thesis addresses several fundamental issues in the field, through experiments and large-scale numerical simulations.

The studies described in Papers I, II, and III investigated methods of controlling the creation of electron beams inside the plasma structure. This is crucial to control the electron bunch quality and reproducibility in a wakefield accelerator.

Although the laser wakefield acceleration technique can be used to accelerate electrons to high energies over short distances, extending the acceleration length is not trivial. A new concept for creating a guiding structure for high-intensity laser pulses is proposed in Paper IV, while Paper V describes an experiment in which it was shown that it is possible to merge two laser wakefield structures into a single structure when they collide at a small angle. This could be used as a means of injecting a new laser pulse to drive the plasma wake when the previous one has become depleted, thus allowing longer acceleration. Another way to increase the acceleration length is to use an electron bunch as a driver for the wakefield. The benefit of this is that, while the laser pulse will travel more slowly than a highly relativistic electron bunch in a plasma, two highly relativistic electron bunches will travel with similar speeds. Therefore, the possibility of using the linear electron accelerator at MAX IV was investigated through computer simulations. The results of these studies are presented in Section 5.6.

A complementary acceleration mechanism called Direct Laser Acceleration, is described in Paper VI. This mechanism affects the generation of X-rays, as also discussed in Section 5.8. Finally, the application of the wakefield accelerator as an X-ray source is described in Papers VII and VIII.

1.1 Structure

Chapter 2 introduces the physics of wakefield acceleration to a more general audience of physicists. Maxwell's equations and Gaussian laser pulses are briefly described, together with basic concepts in plasma physics. The second part of the chapter introduces the concept of wakefield acceleration and the way in which accelerated electrons emit X-rays. The next two chapters describe the scientific methods used for the work presented in this thesis. Chapter 3 introduces the simulation methods used, and the simulation code used by the author is described. Chapter 4 describes the multi-terawatt laser system at the Lund Laser Centre, followed by a description of different diagnostics used to characterize the laser and the laser wake-field acceleration experiments performed. In Chapter 5 the studies performed during the course of this work are presented.

Chapter 2

Electromagnetism, Plasmas and Wakefield Acceleration

A dynamic mess of jiggling things

2.1 High-intensity laser pulses

A central set of equations in this field is Maxwell's equations, which relate the electromagnetic quantities, the electric field, $\mathbf{E}$, the magnetic field, $\mathbf{B}$, the current density, $\mathbf{J}$ and the charge density, ρ, to each other through the speed of light, c, and the vacuum permittivity, ϵ_0. The equations are reproduced here in their differential form:

$$\begin{aligned} \text{Faraday's law} \qquad & \nabla \times \mathbf{E} = -\frac{\partial \mathbf{B}}{\partial t} \\ \text{Ampere's law} \qquad & \nabla \times \mathbf{B} = \frac{\mathbf{J}}{\epsilon_0 c^2} + \frac{1}{c^2}\frac{\partial \mathbf{E}}{\partial t} \\ \text{Gauss's law} \qquad & \nabla \cdot \mathbf{E} = \frac{\rho}{\epsilon_0} \\ \text{Gauss's law for magnetism} \qquad & \nabla \cdot \mathbf{B} = 0. \end{aligned}$$

$\mathbf{E}$ and $\mathbf{B}$ can be expressed as the derivative of a vector potential, $\mathbf{A}$, and a scalar potential ϕ in the following relations:

$$\begin{aligned} \mathbf{E} &= -\nabla\phi - \frac{\partial \mathbf{A}}{\partial t} \\ \mathbf{B} &= \nabla \times \mathbf{A} \end{aligned}$$

In vacuum, ϕ is constant and therefore $\nabla\phi$ is $\mathbf{0}$.

In this chapter, and throughout the simulations performed and described in this thesis, it is assumed that the laser pulse can be described by a Gaussian distribution, both temporally and spatially. The vector potential of a temporal and spatial Gaussian laser pulse in vacuum can be described as a function of the propagation coordinate,

x, the radial distance from the axis, r and the time, t:

$$A(x,r,t) = A_0 f(x,t)\frac{W_0}{W(x)}\exp\left(-\frac{r^2}{W^2(x)}\right)\exp\left(i\left[\omega t - kx - k\frac{r^2}{2R(x)} + \xi(x)\right]\right) + \text{c.c.}$$

where c.c. refers to the complex conjugate, and the envelope function $f(x,t) = \exp\left(-(x-ct)^2/(c\tau_{\mathrm{L}})^2\right)$. This equation introduces a number of important parameters for a laser pulse. A_0 is the peak value of the vector potential, τ_L is the pulse duration, ω is the angular frequency of the laser, $k = 2\pi/\lambda$ is the laser wavenumber, and λ is the wavelength. The beam radius is denoted $W(x) = W_0\sqrt{1+(x/x_R)^2}$, the radius of curvature $R(x) = x(1+(x_R/x)^2)$, $\xi(x)$ is the Gouy phase shift, and the beam radius at the focus is $W_0 = \sqrt{\lambda x_R/\pi}$. $x_R = \pi W_0^2/\lambda$ is the Rayleigh length.

The normalized vector potential, a, provides a measure of the strength of the focused laser pulse, the peak value of which, a_0, is often used. It is given by:

$$a = \frac{q_e A}{m_e c} = \sqrt{\frac{q_e^2}{2\pi^2\epsilon_0 m_e^2 c^5}\lambda^2 I} \approx 0.85\ \lambda\ [\mu\text{m}]\ \sqrt{I\ [10^{18}\text{W/cm}^2]},$$

where q_e is the electron charge and m_e is the electron mass. The right hand side of the equation is given in practical units, where the value is supposed to be inserted with the unit given in square brackets. The benefit of using a value normalized to the electron properties is that the value gives direct information on the interaction. For example, an electron interacting with a laser pulse with $a_0 = 1$ will have a normalized momentum $p/(m_e c)$ of one, meaning that the kinetic energy is the same as the rest mass, and therefore the interaction is relativistic.

For a transform-limited Gaussian laser pulse, the frequency bandwidth, $\Delta\nu$, and the FWHM pulse duration, τ_{FWHM}, are related. The minimum frequency-time product is limited to $\Delta\nu\tau_{FWHM} = 0.44$. An important implication of this is that a broader bandwidth is required to create shorter pulses.

2.1.1 Field ionization

The acceleration medium (typically hydrogen or helium) is assumed to be ionized by the front of the laser pulse in the experiments discussed here. There are many processes through which atoms and molecules can be ionized. The dominant ionization process in laser pulses arises from the strong oscillating electric fields.

If the force exerted on a bound electron by the laser electric field is stronger than the force binding the electron to the nucleus, a phenomenon called over-the barrier-ionization (OTBI) occurs. In a laser pulse, OTBI takes place when the intensity is above the appearance intensity, I_{app}. The appearance intensity can be calculated by equating the peak electric field of a laser pulse with the field binding the electron to the ion [6]. The intensity required to ionize an electron bound with an ionization energy $\mathcal{E}_{ion}$ which, when ionized, creates an ion with charge state Z is:

$$I_{app} = \frac{c\mathcal{E}_{ion}^4}{128\pi Z^2 q_e^6}, \tag{2.1}$$

Table 2.1 gives the ionization energies, appearance intensities and the corresponding normalized vector potentials for some of the ion species used in the experiments

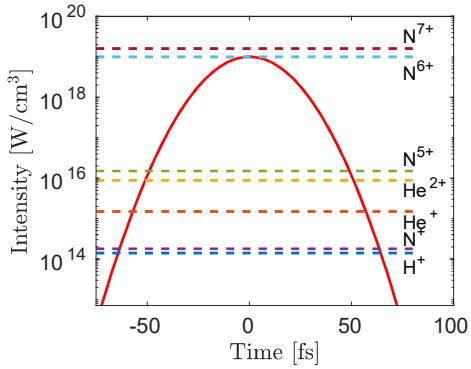

Figure 2.1: A 30 fs Gaussian laser pulse with a peak intensity of 10^{19} W/cm^3. The appearance intensity required for OTBI for different ion species is indicated by the dashed lines. OTBI will occur at the time at which the dashed lines meet the curve describing the intensity of the laser pulse.

described in this thesis. The appearance intensities required for the same ions are compared to the intensity of a 30 fs Gaussian laser pulse as a function of time in Figure 2.1. The peak intensity of the laser pulse is 10^{19} W/cm^2.

2.1.2 Charged particles

A particle with charge q, subject to an electromagnetic field experiences a force $\mathbf{F} = q(\mathbf{E} + \mathbf{v} \times \mathbf{B})$ called the Lorentz force. In a plane wave $|\mathbf{B}| = |\mathbf{E}/c|$. For low light intensities interacting, for example with electrons, the magnetic part of the force is significantly weaker than the electric. As the velocity perpendicular to the magnetic field of the electron approaches the speed of light, $|\mathbf{v} \times \mathbf{B}| \to |\mathbf{E}|$ and both fields play a similar role. When the fields in a laser pulse accelerate the electron to velocities close to the speed of light, the intensity is called relativistic. For convenience, a normalized velocity $\beta = v/c$ is often used. The electrons interacting with the main part of the laser pulse will gain sufficient energy for relativistic effects to be important.

The accelerated electrons studied in this work were highly relativistic. This means that $\beta \approx 1$ and is no longer a convenient way to characterize the electrons. Instead, the Lorentz factor, $\gamma = 1/\sqrt{1-(v/c)^2} = 1/\sqrt{1-\beta^2}$, is used. It is a measure of the total energy of the particle, normalized to the energy corresponding to its rest mass $\mathcal{E} = mc^2$. For example, for a particle at rest, $\gamma = 1$. For a particle with $\gamma = 2$, the

Table 2.1: Table giving data on the ion species used in the work presented in this thesis, including the ionization energy, the intensity required to reach the OTBI regime and the corresponding normalized vector potential for a laser wavelength of 0.8 µm.

Created ion	$\mathcal{E}_{ion}$ [eV]	I_{app} [W/cm^2]	a_{app}
H^+	13.6	$1.4 \cdot 10^{14}$	0.01
He^+	24.6	$1.5 \cdot 10^{15}$	0.03
He^{2+}	54.4	$8.8 \cdot 10^{15}$	0.06
N^+	14.5	$1.8 \cdot 10^{14}$	0.01
N^{5+}	97.9	$1.5 \cdot 10^{16}$	0.08
N^{6+}	552.1	$1.0 \cdot 10^{19}$	2.20
N^{7+}	667.9	$1.6 \cdot 10^{19}$	2.75

kinetic energy is equal to the rest mass and it is travelling at 87 % of the speed of light, and an electron with $\gamma = 400$ moves at 99.9997 % of the speed of light.

2.2 Plasmas

As is clear from a previous section, high-intensity laser pulses will ionize the material with which they interact.

The outer electron shells will be ionized already at the leading edge of the laser pulse. Thus, the main part of the laser pulse will interact with a plasma. The phenomena described in this section can be found in most basic plasma physics textbooks (e.g. [7]).

2.2.1 Plasma parameters

Unlike the other states of matter, the particles in a plasma will couple to other particles over a significant distance through the electromagnetic fields. Therefore, they are not limited to nearest neighbour interactions. In most cases, a plasma consists of electrons and ions. The phenomena described below applies to both species, but due to their difference in mass, the electron distribution defines the interaction between the plasma and light. Therefore, the parameters given below are for the electron part of the plasma.

The displacement of charge in a plasma will start a collective oscillation. The oscillation frequency, ω_p, is called the plasma frequency. For electrons with charge q_e and a mass m_e in a background electron density n_e, ω_p, can be expressed as:

$$\omega_p = \sqrt{\frac{n_e q_e^2}{m_e \epsilon_0}}. \tag{2.2}$$

This oscillation can be triggered by an electromagnetic wave. The plasma electrons will be accelerated by the electric fields according to $F = m\ddot{\mathbf{r}} = q_e\mathbf{E}$. The motion of the electrons will cause a current density $\mathbf{J} = n_e q_e \dot{\mathbf{r}}$. The behaviour of a monochromatic plane wave, with angular frequency ω and wavenumber $k = 2\pi/\lambda$, can be studied by combining the expressions above with Ampere's and Faraday's laws. The following relation between ω and the wave vector $\mathbf{k}$ in the propagation direction can thus be derived

$$\omega^2 = \omega_p^2 + k^2 c^2. \tag{2.3}$$

This relation is called the dispersion relation, from which the phase velocity ($v_p = \omega/k$) and the group velocity ($v_g = \partial\omega/\partial k$) can be retrieved. Expressions for the corresponding refractive indices η are:

$$\eta = \frac{c}{v_p} = \sqrt{1 - (\omega_p/\omega)^2} \tag{2.4}$$

for the phase velocity and

$$\eta_g = \frac{c}{v_g} = \frac{1}{\sqrt{1 - (\omega_p/\omega)^2}}. \tag{2.5}$$

for the group velocity. Note that the phase velocity is greater than c since $\eta < 1$ and the group velocity will be less than c since $\eta_g > 1$. If $\omega_p > \omega$, the refractive index is imaginary, and the electromagnetic wave cannot propagate through the plasma. The electron density corresponding to this limit is called the critical density and is defined as:

$$n_c = \frac{\omega^2 \epsilon_0 m_e}{q_e^2}. \tag{2.6}$$

In other words, at this density the electrons oscillate at the same frequency as the electromagnetic wave. Plasmas with a density below the critical density are usually referred to as underdense plasmas, and this is the regime in which laser wakefield acceleration is performed. Underdense plasmas can be generated from low-density matter such as gases. Overdense plasmas are usually studied in experiments involving the interaction of light with solids or liquids.

The last phenomena in this section is the ponderomotive force. This is an effect that can be intuitively understood by considering an oscillating electric field that is becoming weaker radially. Imagine an electron that is accelerated towards a region with weaker fields. As the electric field shifts and the electron is accelerated back, the force is weaker than it was at the previous position. Therefore, the electron does not return to its original position. As this process is repeated, the electron slowly drifts away from the strong field region towards a region with lower fields. In the low-intensity case, it can be shown that the ponderomotive force, which is an average force, is described by:

$$\frac{d\mathbf{p}}{dt} = -\frac{q^2}{2\omega^2 m} \nabla \langle \mathbf{E}^2 \rangle \tag{2.7}$$

for a particle with charge q and mass m. Here the brackets indicate the time average over a laser cycle. For relativistic intensities, the expression above can be generalized to [8]:

$$\frac{d\mathbf{p}}{dt} = -\frac{q^2}{2m\langle\gamma\rangle} \nabla \langle \mathbf{A^2} \rangle \tag{2.8}$$

The force is proportional to the gradient of the intensity. Furthermore, the force itself is inversely proportional to the mass of the particle, which means that it is 1836 times stronger for an electron at rest than for a proton. Note that the force does not differ with the sign of the charge.

2.2.2 The Vlasov equation

In the regime where the plasma is governed by collective effects, the function $f(\mathbf{r}, \mathbf{p}, t)$, describing the distribution of particles in space ($\mathbf{r}$), momentum ($\mathbf{p}$) and time (t), is described by the Vlasov equation:

$$\frac{\partial f}{\partial t} + \mathbf{v} \cdot \nabla f - q\left(\mathbf{E} + \mathbf{v} \times \mathbf{B}\right) \cdot \frac{\partial f}{\partial \mathbf{p}} = 0. \tag{2.9}$$

When coupled to Maxwell's equations, this provides a model suitable for describing wakefield acceleration. Each individual species should satisfy this equation. For example, to model a hydrogen plasma adequately, both the electrons and the protons must be modelled.

In the studies on wakefield acceleration described in this thesis, the effect of the ions was limited to provide a static background, making the plasma quasi-neutral. This is motivated by the fact that the acceleration of the ions induced by the ponderomotive force is almost 3.4 million times smaller than for electrons. During the time taken for the laser pulse to pass, the ions hardly move at all. However, it has recently been suggested, that the ion motion plays a role in some specific acceleration scenarios [9]. Also, for lasers with $a_0 \gg 1$, (i.e. above the intensities studied in this thesis) the ponderomotive push on the ions will affect the physics.

2.3 Wakefield acceleration

All the papers included in the thesis except Paper IV describe studies of wakefield acceleration and its applications. A short introduction to key phenomena in wakefield acceleration is given in this section. The topic is covered more thoroughly in a review article on the subject [10]. In order to excite a density wave in a plasma, a displacement force is needed. In wakefield acceleration, the ponderomotive force resulting from a high-intensity laser pulse or the electric fields originating from a dense relativistic electron bunch is typically used to excite the wave. The electromagnetic fields associated with the plasma density wave in the wake of the displacement force can accelerate charged particles. In this section, a laser driver is used as an example. In wakefield acceleration, the speed of the driver determines the propagation speed of the plasma wave, thus a plasma wavelength λ_p can be defined. The velocity of the driver, i.e. the group velocity of the laser pulse v_g, is often very close to the speed of light, such that $\lambda_p = 2\pi c/\omega_p$.

2.3.1 Linear plasma waves

For a weak, non-relativistic laser pulse, $a_0 \ll 1$. Assuming a cold plasma fluid model, the small electron plasma density perturbation δn can be described by:

$$\left(\frac{\partial^2}{\partial t^2} + \omega_p^2\right)\frac{\delta n}{n_0} = c^2 \nabla \langle a^2 \rangle \tag{2.10}$$

where $\langle a^2 \rangle$ is the time average over a laser cycle of the squared laser vector potential, and n_0 is the background electron density. Note that the differential equation takes the form of a forced harmonic oscillator. This problem can be solved analytically [11, 12], and it can be shown that a solution to this differential equation is:

$$\frac{\delta n}{n_0} = \frac{c^2}{\omega_p}\int_0^t \sin[\omega_p(t-t')]\frac{\nabla a^2(\mathbf{r},t')}{2}dt' \tag{2.11}$$

for any laser driver shape. The electric fields can be retrieved from the density through Poisson's equation. For a Gaussian driver pulse located at $x = 0$, a wavelength centred at $\lambda = 800$ nm, a pulse duration $\tau_L = 14$ fs, a peak normalized vector potential $a_0 = 0.05$ and a FWHM width of 14 μm in a background density of 10^{19} cm^{-3}, the solution [13] for the longitudinal and the radial electric field , E_x and E_r, is shown in Figure 2.2. To significantly accelerate a beam of charged particles, they must not only experience an accelerating field, but also be kept on axis by a focusing force. The

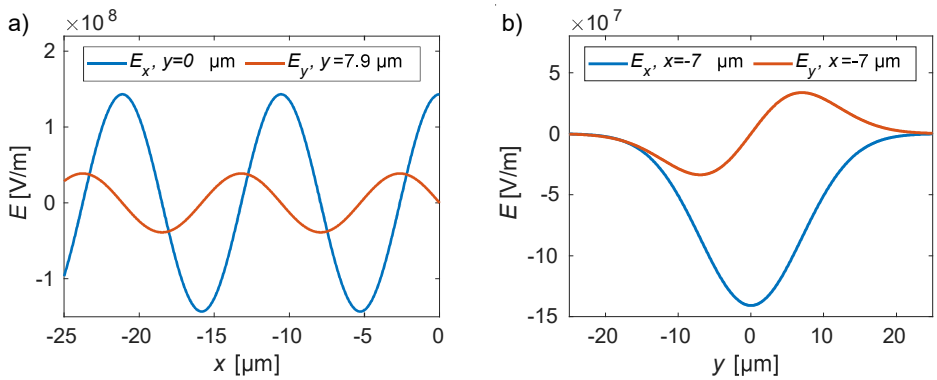

Figure 2.2: The electric fields of a linear plasma wave excited by a laser pulse. The line-out of the longitudinal electric field, E_x, is shown in blue, and the transverse electric field, E_y, is shown in red. a) Line-outs along the propagation direction x. E_x at $y = z = 0$ μm and E_y at $z = 0$ μm, $y = 7.9$ μm (the maximum field value). As can be seen, the fields are out of phase by $\pi/2$. Note that for a charged particle, only a region of a total length $\lambda_p/4$ is both accelerating and focusing. b) Line-outs along a transverse direction y. Both fields at $x = -7$ μm and $z = 0$ μm.

focusing force may be a radial electric or an azimuthal magnetic field. Note that for the linear regime presented here, the fields are focusing and accelerating for a quarter of the plasma wavelength.

2.3.2 Non-linear plasma waves

A non-linar plasma wave can be excited by a strong laser pulse ($a_0 \gtrsim 1$). A differential equation can be constructed for a 1D wave in this regime [11, 12, 14]. To do this, it is useful to transform the coordinates into a new coordinate base, $\xi = x - ct$, which moves with the laser pulse. The normalized velocity of the plasma wave is denoted β_p, and its corresponding Lorentz factor, γ_p, is also used. k_p is the corresponding plasma wavenumber. In this comoving coordinate, the 1D wave differential equation for the normalized electric potential ($\phi = q_e\Phi/(m_e c^2)$) can be written [14]

$$\frac{\partial^2 \phi}{\partial \xi^2} = k_p^2 \gamma_p^2 \left[\beta_p \left(1 - \frac{1 + a^2}{\gamma_p (1 + \phi)^2} \right)^{-\frac{1}{2}} - 1 \right]. \tag{2.12}$$

This differential equation is solved using a numerical solver. The resulting density modulations and longitudinal electric fields are presented in Figure 2.3 for two different a_0, in a background plasma density of 10^{19} cm^{-3}. Note that in Figure 2.3a), $a_0 = 1$, and the fields are no longer purely sinusoidal, as in the linear case shown in Figure 2.2. In Figure 2.3b), $a_0 = 2$, the fields are sawtooth-like, and the density modulations are strongly peaked. The plasma wavelength increases with the driver strength due to the increase in relativistic mass originating from the passage of the electrons over the driver pulse.

Laser wakefield acceleration is sensitive to the dimensionality of the problem. For example, the laser evolution is very different in one, two and three dimensions. In

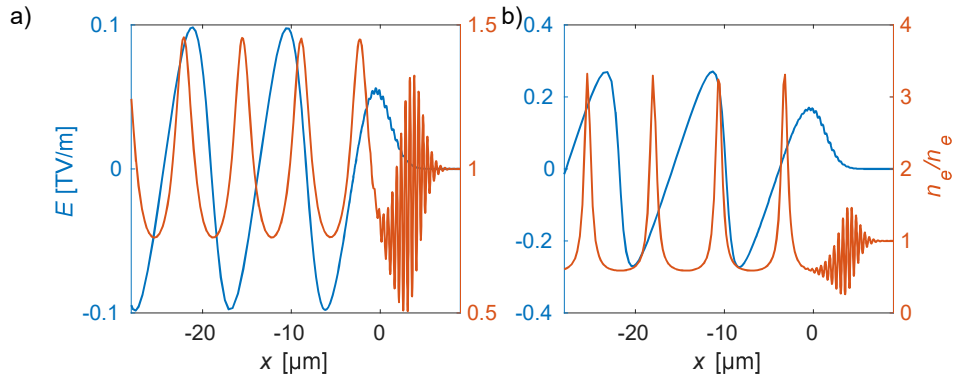

Figure 2.3: The longitudinal electric field (blue) and the density modulation in a non-linear plasma wave for two different Gaussian laser pulses with $\tau_L = 13$ fs in a background plasma density of $n_e = 10^{19}$ cm^{-3}. In a) $a_0 = 1$, and in b) $a_0 = 2$. Note that the plasma wavelength is longer with the higher value of a_0, which is due to the relativistic mass increase of the plasma electrons.

1D, the intensity can only increase if the pulse is compressed in time. In 2D, it can also focus in one dimension, while in 3D, it focuses in two dimension, resulting in a much faster increase in intensity. Therefore, a full 3D model is needed to properly investigate the physics of laser wakefield acceleration. Furthermore, the fluid model used to obtain the differential equations in Equation (2.10) and (2.12) is not valid in the multidimensional non-linear regime. Already in 2D, the fluid-model breaks down due to trajectory crossing. A kinetic model is therefore required to simulate important effects such as electron injection, see Section 2.3.5.

A code solving the Vlasov equation coupled with Maxwell's equation, implemented in quasi-cylindrical geometry, was used to model the physics of laser wakefield acceleration. The method used to solve the system of equations is called the particle-in-cell (PIC) method. The method and the simulation code used are described more detail in Chapter 3.

Figure 2.4a) shows a comparison between the model defined by Equation (2.12) and a 1D PIC code. It can be seen that the results of the model and the PIC simulation are almost identical. Figure 2.4b) shows the corresponding results in three different dimensionalities. Note that the electron density peak is closer to the laser pulse in higher dimensions. This is due to the fact that the electrons in one dimension are forced to pass the peak of the laser pulse, and will therefore increase their apparent mass more than in two dimensions, where the electrons avoid passing over the peak of the laser pulse. In three dimensions, the electrons are free to avoid the laser pulse in two dimensions, decreasing the potential the electron passes even more. This is another example of why three dimensions are needed to properly model wakefield acceleration.

2.3.3 The bubble regime

In the strongly non-linear regime, it is possible to reach almost complete cavitation of electrons behind the laser pulse in three dimensions. This is achieved using a high-

intensity laser pulse ($a_0 > 2$) with a width matched to the plasma wavelength, and a longitudinal length shorter than the plasma wavelength. This is referred to as the bubble regime [15] as the electron density structure is similar to a bubble. This regime is also referred to as the blow-out regime [16], which was originally investigated with plasma waves excited by an electron bunch driver.

Figure 2.5 a) shows a slice of the electron density where the bubble structure is clearly visible. As the driving laser displaces the plasma electrons in its path, a current is initiated that flows around the ion cavity left behind it. These currents give rise to very strong electromagnetic fields. The magnetic field perpendicular to the plane, B_z, is shown in Figure 2.5b). This field will act with a focusing force on an electron travelling close to the speed of light towards the laser driver. Figure 2.5c) shows the radial electric field E_r. Note that the fields are focusing for an electron inside the entire bubble. Figure 2.5d) shows the longitudinal field E_x. In the rear half of the bubble, this field is accelerating for electrons.

2.3.4 Laser pulse evolution

A crucial factor in a laser wakefield accelerator is the evolution of the laser pulse when it propagates in a plasma. To guide a short, intense laser pulse in a plasma, it is necessary to modulate the refractive index. For plasma densities $n_e \ll n_c$ the change in refractive index is proportional to the change in plasma density. A laser pulse with $1/e^2$ spot-size W_0 will be guided if the change in density is $\Delta n_e = (\pi r_e W_0^2)^{-1}$ over the spot size [17], where $r_e = 2.818 \cdot 10^{-15}$ is the classical electron radius. This type of guiding is further discussed in Section 5.4. It can also be guided through the change in apparent mass of the electrons in the strong laser fields [18]. For this to be possible, the power of the laser must be above a critical power [19]

$$P_{crit} = \frac{8\pi\epsilon_0 m_e^2 c^5}{e^2}\frac{n_c}{n_e} \approx 17[\mathrm{GW}]\frac{n_c}{n_e} \tag{2.13}$$

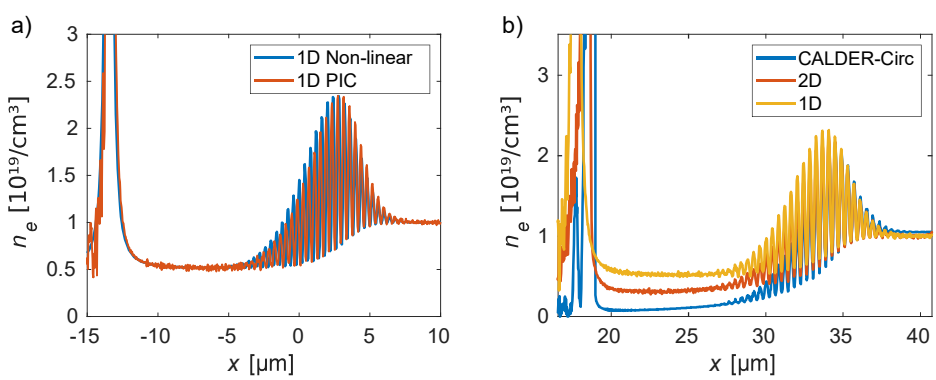

Figure 2.4: a) Comparison between a 1D PIC simulation and the solution to Equation (2.12) for a laser with $a_0 = 4$ and $\tau_p = 16.5$ fs. b) Similar comparisons between the plasma wavelengths for 1, 2 and 3 dimensions. It can be seen that the plasma wavelength is longer in lower dimension-space. The laser spot size in 2D and 3D (Calcer-Circ) simulation was 9.5 μm FWHM.

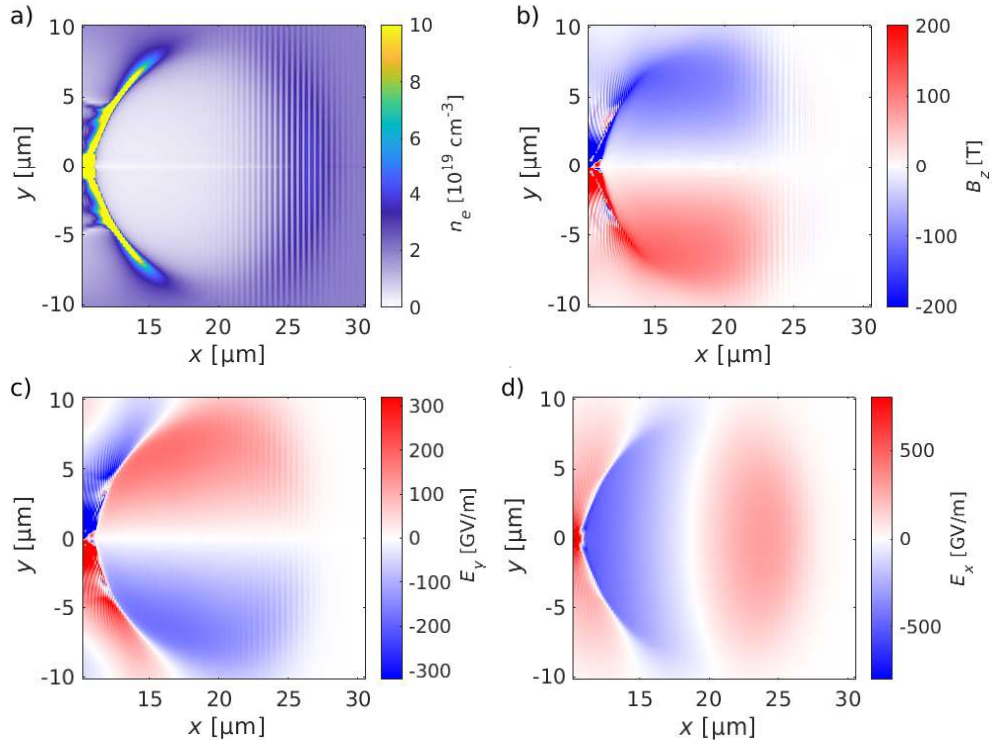

Figure 2.5: Data from a PIC simulation of a laser pulse with a normalized vector potential $a_0 = 4$, FWHM laser pulse width of 9.5 µm, and a FWHM duration of 16.5 fs. The distribution of the electron density, n_e, in a plane through the laser propagation axis is shown in a), and the magnetic field-component B_z is shown in b). The radial and longitudinal electric fields E_y and E_x are shown in c) and d), respectively.

For a laser pulse with normalized vector potential a, an external density modulation Δn_e and laser-induced modulation ∂n_e, the refractive index, η, in the plasma can be expanded as [10, 17]:

$$\eta_r = 1 - \frac{\omega_p^2}{2\omega^2}\left(1 - \frac{a^2}{2} + \frac{\Delta n_e}{n_e} + \frac{\partial n_e}{n_e}\right). \tag{2.14}$$

At the front of the laser pulse, the induced density modulation ∂n_e and the relativistic mass effect arising from the vector potential a, will almost cancel each other. Therefore, the front of the laser pulse will not be self-guided and external guiding is thus needed. However, the laser pulse resonantly excites the plasma wave when $P \approx P_{crit}$ and the laser size is matched to plasma density, and almost complete cavitation of the plasma electrons occurs behind the laser pulse, which creates a guiding structure for the back part of the laser pulse. This is what is referred to as the bubble regime and it gives rise to a refractive index structure, as shown in Figure 2.6a). The laser pulse is located at the front of the bubble, and the location along the axis can be deduced from 2.6 b). The refractive index is calculated taking the relativistic mass of the electron into account, but the effect of the azimuthal magnetic field in the bubble

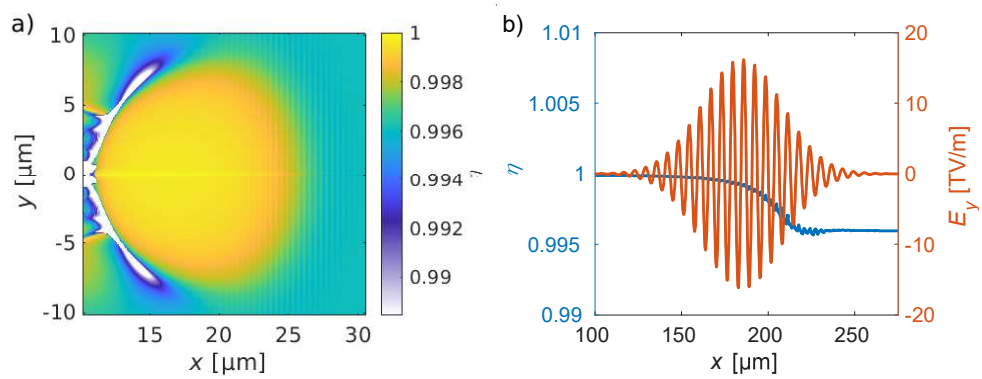

Figure 2.6: a) The refractive index, η, in the bubble as experienced by an 800 nm laser pulse. The plasma and laser parameters are the same as in Figure 2.5. Inside the bubble, the laser will experience a waveguide. If the laser pulse is longer than the bubble, it will be self-modulated when experiencing the strong refractive index at the back of the bubble. At the front of the bubble, the laser pulse experiences a refractive index gradient. b) The on-axis refractive index from the same bubble over the duration of the laser. As can be seen, the front of the laser pulse experiences a refractive index gradient. The gradient induces a varying phase velocity within the laser pulse, leading to frequency broadening.

is neglected. Several features can be observed. The width of the bubble in the radial direction (y in the plot), induces a waveguide structure for the pulse, which changes from vacuum-like properties in the bubble, to electron plasma outside. This structure effectively guides the back of the pulse. Furthermore, the strongest modulations of the refractive index is at the back of the bubble.

The front of the laser pulse will continuously experience a refractive index gradient, as shown in Figure 2.6b). The phase velocity will therefore vary inside the laser pulse. This will cause frequency broadening due to self-phase modulation of the laser pulse, eventually leading to self-compression of the pulse in time. The back of the laser pulse inside the bubble will experience a vacuum-like environment, since the ion plasma frequency is much lower than that of the laser.

Figure 2.7a) shows the electric field of the laser pulse on the propagation axis at two different times obtained from a simulation. As can be seen, the peak field of the laser has increased, mainly due to the focusing effect. The temporal shape is also modified by the interaction with the plasma. Figure 2.7b) shows the spectrum for both pulses, where it can be seen that the spectrum is broadened after propagation in the plasma.

In the matched regime, proposed by Lu *et al*, [20–22], the laser pulse, if properly matched according to $W_0 \approx 2c\sqrt{a_0}/\omega_p$, will guide itself inside the bubble, and the front of the laser pulse will be depleted before it diffracts.

An experimental problem with matching the laser pulse to the plasma is often that the laser power is not high enough to maintain a relativistic intensity over a spot size that is smaller than the length of the pulse. This is a requirement for keeping the bubble formation at the back unperturbed by the laser, so that the electron bunch is not affected by the electromagnetic fields of the laser. A study on the effect on the electron bunch when the laser pulse overlaps with the electron beam is presented

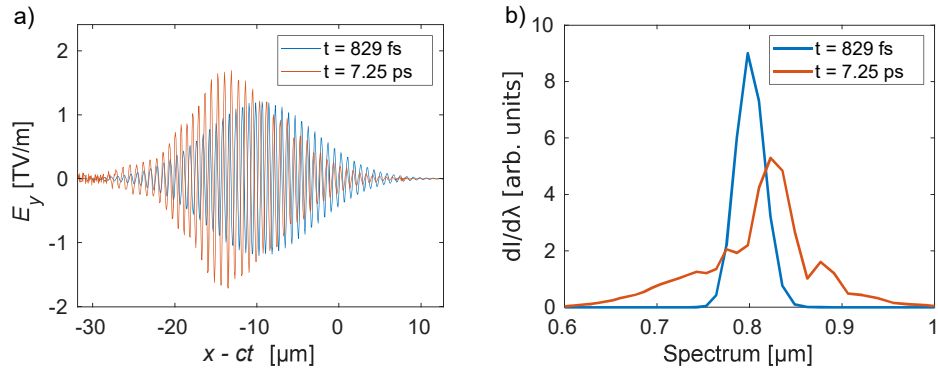

Figure 2.7: a) E_y at two different times as a function of position in the frame moving with the speed of light, obtained from simulations. It can be seen that the longitudinal shape of the laser pulse is modified as it evolves in the plasma. b) The spectrum of the laser pulse, where significant frequency broadening resulting from the plasma propagation can be seen.

in Paper VI. The laser evolution outside the matched regime is further discussed in Chapter 5.

2.3.5 Trapping of electrons

It is possible to create an electron bunch from the background electrons in the plasma by *trapping* or *injecting* electrons in the plasma wave. To elucidate this process, a 1D Hamiltonian model of the electrons in the plasma will be considered. The model is based on the 1D fluid description of the plasma described above in Section 2.3.2. In the electric potential ϕ, the Hamiltonian for a single electron is: $H = \gamma - \phi(x - v_g t)$, which can be written in terms of the normalized transverse momentum $u_\perp = p_\perp/(m_e c)$ and the normalized longitudinal momentum u_x, as: $H = \sqrt{1 + u_\perp^2 + u_x^2} - \phi(x - v_g t)$. A new Hamiltonian can be defined by transforming the coordinates to $\xi = x - ct$. This Hamiltonian can be solved for the longitudinal momentum $u_x = \beta_p \gamma_p^2 (H_0 + \phi) \pm \gamma_p \sqrt{\gamma_p^2 (H_0 + \phi)^2 - \gamma_\perp^2}$. This equation defines a trajectory in phase space for a given Hamiltonian, H_0. Three types of trajectories are particularly interesting in the non-linear plasma wave. These trajectories are shown in Figure 2.8. The y-axis is logarithmic, and the longitudinal momentum is shifted to avoid negative values on the logarithmic scale. The potential fluid model setup is the same as that used to obtain the results shown in Figure 2.3b). The first orbit is an electron starting at rest far from the driver. For this electron, $H_0 = 1$, and its orbit is referred to as the fluid orbit. The orbit is shown as a black line. This orbit is not trapped, and it oscillates in energy as it passes the wakefield. The second interesting orbit is the separatrix orbit, which is the orbit that separates the trajectories between the trajectories that oscillate with the wakefield as it passes, and the trapped trajectories that travels with the wakefield. It is found at the minimum of the potential, ϕ_{min}, at a node of the electric field, for a particle moving at the velocity of the plasma wave. The Hamiltonian for the separatrix is $H_{sep} = \sqrt{1 + a(\xi_{min})^2}/\gamma_p - \phi_{min}$. The trajectory for this Hamiltonian is shown in red. The third type of trajectory is those with $H \leq H_{sep}$. Electrons with

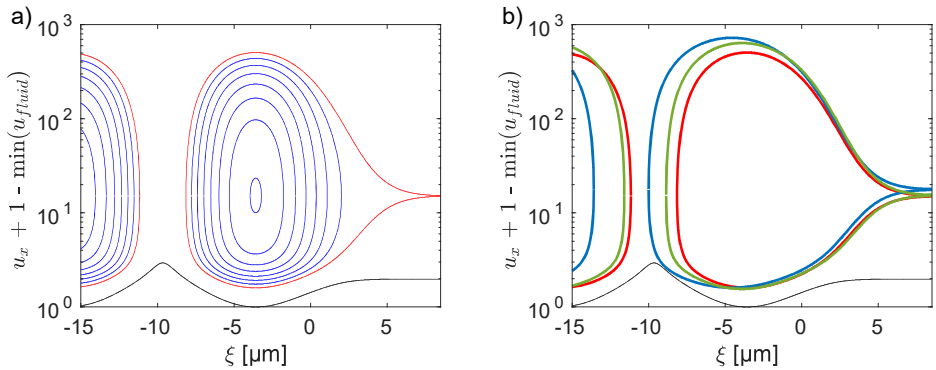

Figure 2.8: a) Phase space trajectories for electrons in the fluid orbit are shown in black, while the separatrix orbit, differentiating free and trapped orbits, is shown in red. Trapped orbits are shown in blue. The plasma wave is excited in a background plasma density of 10^{19} cm^{-3} with a 13 fs laser pulse, with $a_0 = 2$. b) In black and red the same trajectories as in a), the blue line corresponds to the separatrix for an electron density $7 \cdot 10^{18}$ cm^{-3} with the same driver pulse. In green the driver pulse $a_0 = 2.3$ but is otherwise identical to a). Both a decrease in electron density and an increase in a_0 can expand the separatrix and trigger injection.

these trajectories are trapped in the plasma wave. Examples of these are shown in blue in Figure 2.8. For the sake of this discussion, *trapping* is defined as the process of placing electrons in a trapped trajectory. This is also commonly referred to as electron *injection*. These terms will be used interchangeably throughout this thesis. For example, density down-ramp injection and density down-ramp trapping refer to the same physical phenomenon.

Electrons can be trapped by changes of the size of the plasma wave. The plasma wave will change, for example, if the driver strength or the background density changes. This is illustrated in Figure 2.8b) where the separatrix is shown for three different cases. The fluid trajectory (black) and the separatrix (red) in 2.8a), with an electron density of 10^{19} cm^{-3} and $a_0 = 2$, is to be compared to the separatrix for the same laser pulse but a background density $7 \cdot 10^{18}$ cm^{-3} (in blue) and for the same background density but instead using a stronger laser pulse with $a_0 = 2.3$. It can be seen that, when the laser pulse increases in intensity, or the background density decreases, the separatrix expands. During this expansion, electrons in a trajectory between the old and new separatrix can be trapped and accelerated. These are the mechanisms behind *self-injection* and *density down-ramp trapping*. In the case of self-injection, expansion is caused by the laser evolution in the plasma, discussed above. In the case of down-ramp trapping, expansion is due to a decrease in background density.

This evolving-bubble trapping mechanism has been studied extensively [23–27] and is the topic of Paper I. It is also included in the discussion in Paper II. In the bubble regime described earlier, the condition for self-injection has been studied as function of the plasma parameters in the rest frame of the bubble. A condition for trapping is defined [28]

$$\frac{c\sqrt{\ln(2\gamma_p^2) - 1}}{\omega_p r_b} \leq \frac{1}{2}. \tag{2.15}$$

If this is fulfilled, the distance an electron travels before it catches up with the bubble, is shorter than the bubble radius r_b, and is therefore trapped. If the scaling parameters for the bubble regime are used [20], this relation relates the bubble radius needed to trigger self-injection in a certain electron plasma density.

Another method of trapping electrons is *ionization-induced injection* [29]. Referring to the trapped trajectories shown in Figure 2.8, ionization injected electrons will be "created" on a trapped trajectory when they are ionized close to the peak of the laser pulse. This process has been described in the literature [30]. A requirement can be defined for trapping of an electron ionized in the potential of the laser pulse. At the front of the bubble, the electric potential is at its maximum at the peak intensity of the laser pulse. The potential then decreases towards the back of the bubble. Thus an electron ionized at the peak of the laser pulses experiences a potential drop. If this drop is large enough, the electron gains enough forward momentum to start co-propagating with the wave and is consequently trapped by the wakefield. More precisely, the difference in normalized electric potential ϕ between the ionization location and the point of lowest potential in the bubble should satisfy

$$\Delta\phi < -1. \tag{2.16}$$

This injection method is used in Papers II, V, VI, VII, and VIII.

The third and last trapping mechanism discussed here is called *colliding pulse injection* (CPI). By colliding the driver pulse with a weaker counter-propagating pulse, background electrons in the plasma can be forced to enter into a trapped trajectory through the ponderomotive force arising from the beat wave between the two pulses [31–34]. The ponderomotive force in the beat wave is given by $F_{x,beat} = -(m_e c^2/\gamma)(\partial/\partial x)a_1 a_2 \cos(2k_L x)$ where a_1 and a_2 are the normalized vector potentials of the colliding laser pulses. The normalized longitudinal momentum can be found in a similar way as in the plasma wave. For CPI, the interesting values are the extrema values of the separatrix in phase space. They depend on the normalized beat wave velocity β_b arising from the difference in laser frequency, the corresponding longitudinal Lorentz factor γ_b, and the transverse $\gamma_{b\perp} = 1 + \hat{a}_0^2 + 2\hat{a}_0\hat{a}_1$ where $\hat{a}_0^2$ and $\hat{a}_1^2$ are the normalized envelopes of the individual pulses. The extrema values read $u_{b\pm} = \beta_b\gamma_b\gamma_{b\perp}(0) \pm 2\gamma_b\sqrt{\hat{a}_0\hat{a}_1}$. Trapping occurs when the beat wave trajectory forms a path from the cold orbit in the wakefield potential, to a trajectory inside the separatrix of the wakefield.

2.3.6 Electron bunches

The quality of an electron bunch is often measured by its size in 6D phase space which includes the three space dimensions x, y, z and their corresponding dimensions in momentum space p_x, p_y, p_z. These quantities are often specified in the space-momentum pairs for the dimensions perpendicular to the propagation direction, y, p_y, and z, p_z. A common measurement of the area they occupy is the normalized trace-space emittance, which compensates for the particle momentum in the propagation direction. The normalized trace-space emittance can be calculated according to [35]:

$$\epsilon_{n,tr,rms} = \frac{\bar{p_x}}{m_0 c}\sqrt{\langle y^2\rangle \left\langle \frac{p_y^2}{p_x^2} \right\rangle - \left\langle y\frac{p_y}{p_x} \right\rangle^2} \tag{2.17}$$

where $\bar{p_x}$ is the average longitudinal momentum and $\langle\rangle$ denotes the second central moment of all particles in the bunch. The propagation direction, x, p_x is usually treated separately in terms of bunch duration (or length) and the energy spread. The effect on these parameters from the down-ramp injection parameters were investigated and described in Paper I.

2.4 Emission of X-rays

An important application of laser wakefield accelerators is as a source of X-rays. The X-ray spectrum is synchrotron-like and the source size is on the order of µm. The X-ray pulse also has a fs-duration [36, 37]. Applications of these X-ray pulses are described in Papers VII and VIII and the characteristics of the X-ray source is presented in Section 5.8. The X-ray radiation origins from a sinusoidal motion performed by the electrons due to the focusing force in the bubble. This oscillation has the characteristics of an harmonic oscillator, if the energy gain of the particle is neglected. This oscillation is referred to as the betatron motion. This motion can be described by an amplitude r_β, and a wave number k_β through $r(x) = r_\beta \sin(k_\beta x)$. Its frequency depends on the background plasma density, and energy the particle, the betatron frequency is

$$\omega_\beta = \frac{\omega_p}{\sqrt{2\gamma}}. \tag{2.18}$$

The radiation properties depend on how large the angle of the electron trajectory is compared to the angle of emission (which scales as $1/\gamma$). Typically for laser wakefield accelerators, the oscillations are large and the radiation is emitted in what is called the wiggler regime [37]. To identify this regime the K-parameter can be introduced where $K = r_\beta \gamma k_\beta$ is the normalized transverse angular momentum of the electron. In the wiggler regime $K \gg 1$.

An accelerated charge emits electromagnetic waves with a power [38]

$$P = \frac{q_e^2}{6\pi\epsilon_0 c^3}\gamma^6(\dot{\beta}^2 - (\beta \times \dot{\beta})^2) \tag{2.19}$$

For an electron in the bubble, the emitted power is [37]

$$P_s = \frac{\pi q_e^2 c}{3\epsilon_0}\frac{\gamma^2 K^2}{\lambda_u^2} \tag{2.20}$$

The radiated power have a quadratic dependence on both the electron energy γ and the K-parameter. The critical energy of the radiation is defined as, $\mathcal{E}_c = \hbar\omega_c = 3/2K\gamma^2 hc/\lambda_\beta$.

Furthermore, the radiated energy per unit frequency ω and unit solid angle Ω in the direction $\mathbf{n}$ is given by the relation [38]

$$\frac{d^2 I}{d\omega d\Omega} = \frac{q_e^2}{4\pi^2 c}\left|\int_{-\infty}^{\infty} \mathbf{n} \times \frac{[(\mathbf{n} - \boldsymbol{\beta}) \times \dot{\boldsymbol{\beta}}]}{(1 - \boldsymbol{\beta} \cdot \mathbf{n})^2} e^{i\omega(t - \mathbf{n}\cdot\mathbf{r}(r)/c)} dt\right|^2. \tag{2.21}$$

For a particle performing betatron oscillations in an ion channel, it can be shown that the emitted radiation is synchrotron-like [36] and the emission is described by

$$\frac{dI^2}{d\omega d\Omega} = N_\beta \frac{3q_e^2}{2\pi^3\epsilon_0 c^3}\frac{\gamma_{x0}^2\zeta^2}{1 + \gamma_{x0}^2\theta^2}\left[\frac{\gamma_{x0}^2\theta^2}{1 + \gamma_{x0}^2\theta^2}\mathcal{K}_{1/3}^2(\zeta) + \mathcal{K}_{2/3}^2(\zeta)\right] \tag{2.22}$$

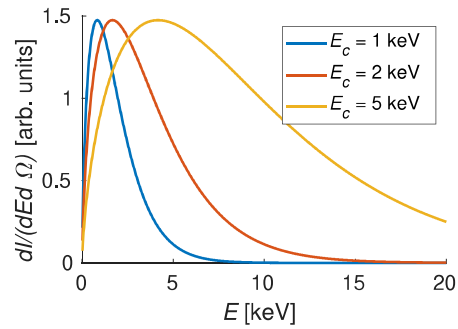

Figure 2.9: Example spectra on axis of synchrotron radiation for different critical energies E_c.

where $\mathcal{K}_{1/3}$ and $\mathcal{K}_{2/3}$ are the modified Bessel functions of the second kind and $\zeta = \frac{\mathcal{E}}{2\mathcal{E}_c}(1+\gamma_{x0}^2\theta^2)^{3/2}$. For emission in the propagation direction, $\theta = 0$, the following dependence can be deduced

$$\frac{d^2I}{(d\mathcal{E}d\Omega)_{\theta=0}} \propto \gamma_{x0}^2 \left(\frac{\mathcal{E}}{\mathcal{E}_c}\right)^2 \mathcal{K}_{2/3}^2\left(\frac{\mathcal{E}}{\mathcal{E}_c}\right) \tag{2.23}$$

A few example spectrum shapes for different values of $\mathcal{E}_c$ are plotted in Figure 2.9. For the wakefield accelerator at the Lund Laser Centre, with $K \approx 10$ (see Figure 5.11), the electron density 10^{19} cm^{-3} and a typical energy is on the order of 100 MeV, the critical energy $\mathcal{E}_c = 3.5$ keV. This agrees with the finding presented in Paper VIII and the results presented in Section 5.8.

Chapter 3

Numerical Tools

Numerical simulations are powerful tools that can provide insight into physical processes that are difficult to study experimentally. Simulations can provide information on any simulated physical property, at any given time, while experimental studies are often limited to projections, or the end results of an experiment. However, it is important to remember that simulations have limitations. Approximations or assumptions are often used, which may not be valid under all conditions. Numerical solvers are not analytical functions, and they will therefore introduce numerical errors. It is therefore important to bear in mind that the simulations we create do not define reality, and new physics "discovered" by simulations should always be treated with skepticism initially. Whether the perceived reality we live in is a simulation or not [39] will unfortunately not be answered, nor further investigated, in this thesis.

This chapter introduces the particle-in-cell (PIC) method, and describes the PIC code CALDER-Circ [40].

3.1 Particle-in-cell simulations

A naive way to simulate a plasma would be to calculate the forces between all the particles individually. However, this is impossible as this is an N-body problem, with a computational cost of N!, where ! represents the factorial operator. In a typical experiment at the Lund Laser Centre a plasma cylinder with dimensions of 50 μm x 50 μm x 2 mm is simulated with a background density of 10^{19} electrons cm^{-3}. This corresponds to $5 \cdot 10^{13}$ electrons in the cylinder. To model the coulomb interaction between all electrons $5 \cdot 10^{13}! \approx 4 \cdot 10^{663233776121645}$ calculations would be needed to be performed each time step. This is an enormous number, and even with state of the art super computers, it is far beyond imaginable to compute even one time step!

Under certain assumptions, plasmas can be modelled using fluid models, for example, the magneto-hydrodynamic model. However, fluid models are limited and cannot by definition model kinetic effects[1]. In high-intensity laser-plasma interactions, kinetic effects must be included, and therefore the fluid models are inadequate. To correctly

[1] Fluid models are limited to modelling the fluid density, fluid velocity, and fluid temperature at one position in time.

model the physics of wakefield acceleration a kinetic model is needed in which particles are free to move in a 6D (x, y, z, p_x, p_y, p_z) phase space. Furthermore, wakefield acceleration occurs in plasmas with a relatively low density and high temperature, which renders the physical effect of binary collisions between particles negligible. Thus, only the collective kinetic effects arising from the plasma fields are required to correctly model the physics. This is the regime in which the Vlasov equation coupled with Maxwell's equations is valid. One way[2] to solve the Maxwell-Vlasov equations is using the PIC method. The electromagnetic fields are discretized in space using a finite-difference method. The fields are known on the nodes of the finite-difference mesh. The distribution function in the Vlasov equation is instead discretized using the characteristic method. In this discretization scheme, it is assumed that the distribution $f(\mathbf{r}, \mathbf{p})$ can be approximated by a finite sum of statistical particles:

$$f(\mathbf{r}, \mathbf{p}) = \sum_{p=1}^{N} W_p \delta(\mathbf{r} - \mathbf{r_p}) \delta(\mathbf{p} - \mathbf{p_p}) \tag{3.1}$$

where W_p is the statistical weight of the numerical particle p, henceforth referred to as a macro-particle, δ is the Dirac delta function, and $\mathbf{r_p}$ and $\mathbf{p_p}$ are the particle position and momentum. Note that previously, the subscript p referred to properties of a plasma, while here it refers to the index of a single macro-particle. It can be shown that since $df/dt = 0$ for the Vlasov equation, the trajectory of this macro-particle corresponds to the trajectory of a real particle occupying the same position in phase space. Without collisions, two physical electrons populating the same region of phase space should follow the same trajectory in time. The macro-particles do no interact with each other directly, but through the electromagnetic fields computed on a mesh.

The PIC method can be summarized as an iterative loop in time, as illustrated in Figure 3.1. For each time step, the fields computed with Maxwell's equations (block a and b in Figure 3.1) are used to push the macro-particles (block c). The macro-particles will in turn contribute to the evolution of the electromagnetic fields through the current generated by the displacement of the macro-particles (block d).

The electromagnetic fields known on the grid, are coupled to the macro-particles from the characteristic discretization method through an interpolation function. The electromagnetic fields F which correspond to the field components $E_x, E_y, E_z, B_x, B_y, B_z$, can be calculated for each macro-particle p by:

$$F_p = F(\mathbf{r_p}) = \sum_j F_j S(\mathbf{R_j} - \mathbf{r_p}) \tag{3.2}$$

where the sum is over all nodes located at position $\mathbf{R}$, and S is the so-called shape function explained in Section 3.2.3.

The first PIC code was developed for hydrodynamic calculations early in the history of computers [41]. It has since been adapted to the field of laser-plasma interactions. A thorough explanation of PIC codes, and how they can be applied to plasmas can be found in a textbook on the subject [42].

[2]There are other methods, such as the so-called Vlasov codes, that solve the Vlasov equation on a finite grid. This is impractical for wakefield acceleration for computational reasons, as the sampled momentum space must be very large.

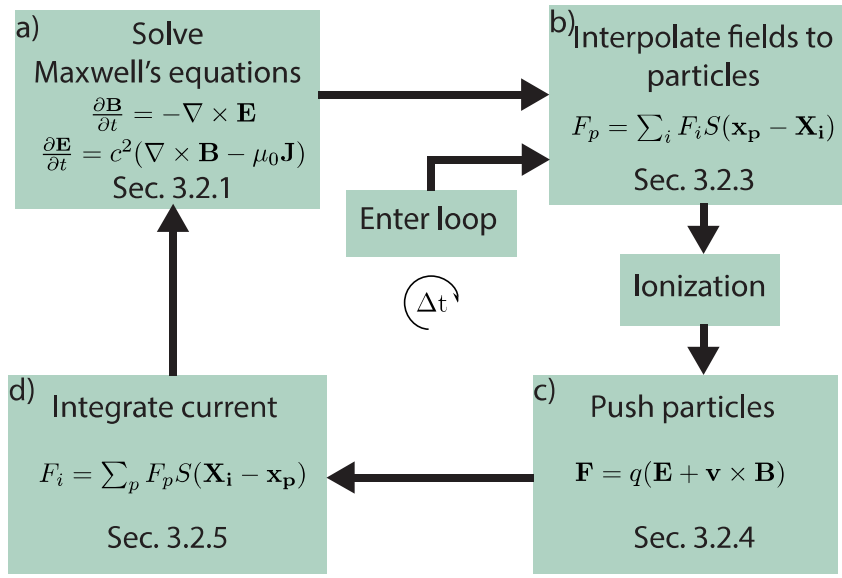

Figure 3.1: A schematic of the particle-in-cell solver described in more detail in this chapter. The PIC loop links the evolution of the macro-particles representing the plasma distribution function to Maxwell's equations discretized on a grid. The electromagnetic fields calculated on the grid are used to push the macro-particles. The current density, arising from the moving charges, is then coupled back to Maxwell's equations. The coupling between the particles and the grid is achieved using shape functions. For a more detailed description of each block in the loop, the corresponding section in this chapter is given in each block.

The PIC method is a powerful tool, and can be applied to systems in which Maxwell-Vlasov equations are valid[3]. Furthermore, effects not described by these equations can often be added through modules, for example, ionization, weak collisions with small scattering angles [43] and quantum electrodynamics (QED) effects. However, the physics has a 6D kinetic nature, and the simulations are therefore computationally expensive. Therefore, PIC simulations are limited to small simulation volumes, which are suitable for intense, short-pulse laser-plasma interactions. To keep the simulation box as small as possible in wakefield acceleration simulations, a moving simulation box is used that follows the driver. Therefore, only the region closest to the laser pulse need be simulated. This is possible because the physics of the electron bunch and the generated X-rays is limited to this region. Due to the computational load, simulations on long time scales are difficult to perform, given, for example, that a laser wavelength should be resolved, which is necessary for laser-plasma interaction phenomena[4]. For example, it is not possible with current super-computers to calculate the effect of the nanosecond pre-pulses of a laser pulse using 6D kinetics with current supercomputers[5]. The pre-pulse was assumed to turn the gas into a plasma in the

[3]Some even claim that it solves the Klimontovich equation.

[4]In some cases, a laser envelope solver can be used, which reduces the resolution required in the simulations.

[5]Simulations of pre-plasmas created by laser pre-pulses can be performed using, e.g., fluid codes.

work described in this thesis.

Today, many PIC codes are used within the laser-plasma interaction community. Examples of these are CALDER, OSIRIS, ELMIS, PICADOR, PICCANTE, PICon-GPU, EPOCH, WARP-X and SMILE. The simulations presented in this thesis, were carried out using a code called CALDER-Circ [40], which will be described in more detail below.

3.2 The PIC code CALDER-Circ

CALDER-Circ is a quasi-cylindrical PIC code that exploits the general cylindrical symmetry of the wakefield acceleration process to reduce the computational load. In cylindrical coordinates, r, θ, x, the azimuthal coordinate, θ, can be represented by a Fourier expansion:

$$\mathbf{F}(r, x, \theta) = \mathbb{R}\left(\sum_{m=0}^{M} \tilde{\mathbf{F}}^{\mathbf{m}}(r, x) e^{-im\theta}\right). \tag{3.3}$$

where F represents any property known on the finite-difference mesh, $\mathbb{R}$ is the real part operator, and $\tilde{\mathbf{F}}$ represents the Fourier coefficient plus its complex conjugate from the $-m$ part of the sum. To represent the θ dimension perfectly, M should approach infinity. However, only $m = 0$ is needed to represent properties that are cylindrically symmetric (such as the wakefield). Furthermore, for a laser pulse in Cartesian coordinates, where x is the propagation direction of the laser pulse, and y is the polarization direction, the fields can be written in cylindrical coordinates as:

$$\mathbf{E}(\mathbf{r}, \mathbf{x}, \theta, \mathbf{t}) = E_y(r, x, t)\hat{y} = E_y(r, x, t)(\cos(\theta)\hat{e}_r - \sin(\theta)\hat{e}_\theta) \tag{3.4}$$

$$\mathbf{B}(\mathbf{r}, \mathbf{x}, \theta, \mathbf{t}) = B_z(r, x, t)\hat{z} = B_z(r, x, t)(\sin(\theta)\hat{e}_r + \cos(\theta)\hat{e}_\theta) \tag{3.5}$$

These fields can be fully represented azimuthally by only the first mode $m = 1$.

Interestingly, the azimuthal sum only has to include $m = 0, 1$ to model the two most important features in laser wakefield acceleration, the wakefield and the laser pulse. In the present work, most of the simulations were performed using 3 modes ($m = 0, 1, 2$), but only 2 modes were used in some cases. Experience shows that 2 modes are sufficient to represent a laser pulse, but the physics at the back of the bubble can be affected, and is sometimes not simulated correctly.

In Fourier-decomposed cylindrical coordinates, Faraday's and Ampere's laws take the form:

$$\frac{\partial \tilde{B}_{r,m}}{\partial t} = \frac{im}{b} r \tilde{E}_{x,m} + \frac{\partial \tilde{E}_{\theta,m}}{\partial x}$$

$$\frac{\partial \tilde{B}_{\theta,m}}{\partial t} = -\frac{\partial \tilde{E}_{r,m}}{\partial x} + \frac{\partial \tilde{E}_{x,m}}{\partial r}$$

$$\frac{\partial \tilde{B}_{x,}}{\partial t} = -\frac{1}{r}\frac{\partial (r\tilde{E}_{\theta,m})}{\partial r} - \frac{im}{r}\tilde{E}_{r,m}$$

$$\frac{1}{c^2}\frac{\partial \tilde{E}_{r,m}}{\partial t} = -\frac{im}{r}\tilde{B}_{x,m} - \frac{\partial \tilde{B}_{\theta,m}}{\partial x} - \mu_0 \tilde{J}_{r,m}$$

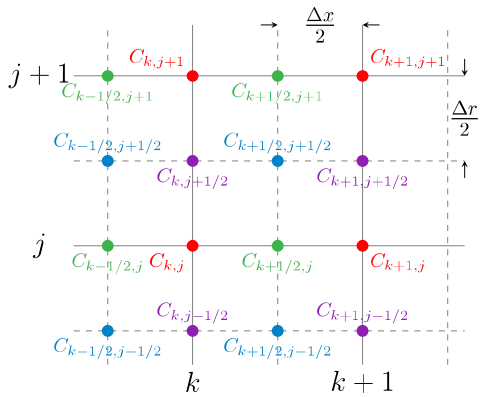

Figure 3.2: Layout of the primal and dual mesh. Components C that are primal in both x and r are shown in red. Components C that are dual in both x and r are shown in blue. Components C that are primal in x and dual in r are shown in purple. Components C that are dual in x and primal in r are shown in green. k represents the position $k\Delta x$, j represents the position $j\Delta r$. Known values for the different mesh nodes are given in Table 3.1

$$\frac{1}{c^2}\frac{\partial \tilde{E}_{\theta,m}}{\partial t} = \frac{\partial \tilde{B}_{r,m}}{\partial x} - \frac{\partial \tilde{B}_{x,m}}{\partial r} - \mu_0 \tilde{J}_{\theta,m}$$
$$\frac{1}{c^2}\frac{\partial \tilde{E}_{x,m}}{\partial t} = \frac{1}{r}\frac{\partial (r\tilde{B}_{\theta,m})}{\partial r} + \frac{im}{r}\tilde{B}_{r,m} - \mu_0 \tilde{J}_{x,m}.$$

To solve the propagation of a laser pulse in vacuum, the EM fields must be known in time and space, such that the spatial and temporal derivative can be used to advance the field in time. However, in the presence of free charge, the current, **J**, is also needed.

3.2.1 The finite-difference time-domain solver

The electromagnetic fields in CALDER-Circ are solved on a finite-difference mesh consisting of cells of the size $\Delta x \times \Delta r$, while time is discretized in steps of Δt. CALDER-Circ uses an adapted Yee solver [44]. Yee proposed a method to obtain centred derivatives in order to obtain a second-order scheme to increase the numerical accuracy of the calculations. He achieved this by implementing a so-called dual mesh. Two grids are shown, in Figure 3.2, one represented by solid lines, and the other by dashed lines, which are displaced by half a cell width with respect to each other. Values of the fields, current and charge density in one direction will be known either on the primal mesh (solid lines) or on the dual mesh (dashed lines). k and j represent the cell number in the x- and r-directions respectively, where $k = x/\Delta x$ and $j = r/\Delta r$. In this way, a centred derivative

$$\Delta_{x,k} F = \frac{F_{k+\frac{1}{2}} - F_{k-\frac{1}{2}}}{\Delta x}$$

can be calculated on the other mesh.

In order to get the same precision for the time derivative, the electric and magnetic fields are not known at the same point in time, their position is shifted in time by $\Delta t/2$. Table 3.1 gives a list of each component of the vectors **E**, **B** and **J** as well as the density, ρ. The dual mesh is illustated in Figure 3.2, and the known fields are listed in Table 3.1.

In CALDER-Circ, a 2D dual mesh is used to represent $\tilde{F}_m(x,r)$. In addition, this component must be solved on the grid for each Fourier mode used. Consequently, the computation cost scales as a 2D code rather than a 3D code when increasing the

Table 3.1: A list of the field values together with the corresponding position in space and time at which they are known. As can be seen, the electric fields (E) are not known at the same time as the magnetics fields (B) and the current, J. The colors refer to the mesh shown in Figure 3.2.

Field	x	r	Time
E_x	Dual	Primal	$n\Delta t$
E_r	Primal	Dual	$n\Delta t$
E_θ	Primal	Primal	$n\Delta t$
B_x	Primal	Dual	$(n+1/2)\Delta t$
B_r	Dual	Primal	$(n+1/2)\Delta t$
B_θ	Dual	Dual	$(n+1/2)\Delta t$
J_x	Dual	Primal	$(n+1/2)\Delta t$
J_r	Primal	Dual	$(n+1/2)\Delta t$
J_θ	Primal	Primal	$(n+1/2)\Delta t$
ρ	Primal	Primal	$n\Delta t$

size of the simulation box. However, it maintains important 3D features such as laser pulse evolution and bubble size.

Effects of discretization

When discretizing Maxwell's equations on the CALDER-Circ dual mesh, the field or current component at time step n, grid node j, k and Fourier mode m can be written as $\tilde{F}^n_{j,m,k}$, where F can be any field or current component. The discretized Maxwell equations are:

$$\frac{\tilde{B}_r{}^{n+\frac{1}{2}}_{j,m,k+\frac{1}{2}} - \tilde{B}_r{}^{n-\frac{1}{2}}_{j,m,k+\frac{1}{2}}}{\Delta t} = -\frac{(D^*_\theta \tilde{E}^n_x)_{j,m,k+\frac{1}{2}}}{j\Delta r} + (D^*_x \tilde{E}^n_\theta)_{j,m,k+\frac{1}{2}}$$

$$\frac{\tilde{B}_\theta{}^{n+\frac{1}{2}}_{j+\frac{1}{2},m,k+\frac{1}{2}} - \tilde{B}_\theta{}^{n-\frac{1}{2}}_{j+\frac{1}{2},m,k+\frac{1}{2}}}{\Delta t} = -(D^*_x \tilde{E}^n_r)_{j+\frac{1}{2},m,k+\frac{1}{2}} + (D^*_r \tilde{E}^n_x)_{j+\frac{1}{2},m,k+\frac{1}{2}}$$

$$\frac{\tilde{B}_x{}^{n+\frac{1}{2}}_{j+\frac{1}{2},m,k} - \tilde{B}_x{}^{n-\frac{1}{2}}_{j+\frac{1}{2},m,k}}{\Delta t} = -\frac{(D^*_r r \tilde{E}^n_\theta)_{j+\frac{1}{2},m,k}}{(j+\frac{1}{2})\Delta r} + \frac{(D^*_\theta \tilde{E}^n_r)_{j+\frac{1}{2},m,k}}{(j+\frac{1}{2})\Delta r}$$

$$\frac{\tilde{E}_r{}^{n+1}_{j+\frac{1}{2},m,k} - \tilde{E}_r{}^{n}_{j+\frac{1}{2},m,k}}{c^2\Delta t} = -\frac{im}{(j+\frac{1}{2})\Delta r}\tilde{B}_x{}^{n+\frac{1}{2}}_{j+\frac{1}{2},m,k} - (D^*_x \tilde{B}^{n+\frac{1}{2}}_\theta)_{j+\frac{1}{2},m,k} - \mu_0 \tilde{J}_r{}^{n+\frac{1}{2}}_{j+\frac{1}{2},m,k}$$

$$\frac{\tilde{E}_\theta{}^{n+1}_{j,m,k} - \tilde{E}_\theta{}^{n}_{j,m,k}}{c^2\Delta t} = (D_x \tilde{B}^{n+\frac{1}{2}}_r)_{j,m,k} - (D_r \tilde{B}^{n+\frac{1}{2}}_x)_{j,m,k} - \mu_0 \tilde{J}_\theta{}^{n+\frac{1}{2}}_{j,m,k}$$

$$\frac{\tilde{E}_x{}^{n+1}_{j,m,k+\frac{1}{2}} - \tilde{E}_x{}^{n}_{j,m,k+\frac{1}{2}}}{c^2\Delta t} = -\frac{(j+\frac{1}{2})\tilde{B}_\theta{}^{n+\frac{1}{2}}_{j+\frac{1}{2},m,k+\frac{1}{2}} - (j-\frac{1}{2})\tilde{B}_\theta{}^{n+\frac{1}{2}}_{j-\frac{1}{2},m,k+\frac{1}{2}}}{j\Delta r} + \frac{il}{j\Delta r}\tilde{B}_r{}^{n+\frac{1}{2}}_{j,m,k+\frac{1}{2}} + \mu_0 \tilde{J}_x{}^{n+\frac{1}{2}}_{j,m,k+\frac{1}{2}}$$

Where the operators are defined as

$$(D_r F)_{j',m,k'} = \frac{F_{j'+\frac{1}{2},m,k'} - F_{j'-\frac{1}{2},m,k'}}{\Delta r}$$

$$(D_x F)_{j',m,k'} = \frac{F_{j',m,k'+\frac{1}{2}} - F_{j',m,k'-\frac{1}{2}}}{\Delta x}$$

$$(D_x^* F)_{j',m,k'} = \alpha_x \left(\frac{F_{j',m,k'+\frac{1}{2}} - F_{j',m,k'-\frac{1}{2}}}{\Delta x} \right) + \delta_x \left(\frac{F_{j',m,k'+\frac{3}{2}} - F_{j',m,k'-\frac{3}{2}}}{\Delta x} \right)$$

$$(D_\theta^* F)_{j',m,k'} = \alpha_\theta \left(-imF_{j',m,k'} \right) - im\beta_{\theta,x} \left(F_{j',m,k'+1} - F_{j',m,k'-1} \right)$$

$$(D_r^* F)_{j',m,k'} = \alpha_r \left(\frac{F_{j'+\frac{1}{2},m,k'} - F_{j'-\frac{1}{2},m,k'}}{\Delta r} \right)$$

$$+\beta_{r,x} \left(\frac{F_{j'+\frac{1}{2},m,k'+1} - F_{j'-\frac{1}{2},m,k'+1}}{\Delta r} + \frac{F_{j'+\frac{1}{2},m,k'+1} - F_{j'-\frac{1}{2},m,k'+1}}{\Delta r} \right)$$

Furthermore, the following conditions are imposed on the coefficients α, β and δ:

$$\alpha_x + 3\delta_x = 1$$

$$\alpha_\theta + 2\beta_{\theta,x} = 1$$

$$\alpha_r + 2\beta_{r,x} = 1$$

For the Yee scheme adapted to CALDER-Circ, $\delta_x = \beta_{\theta,x} = \beta_{r,x} = 0$.

Discretizing Maxwell's equations on a finite-difference grid will affect the dispersion relation. For the Yee solver it can be shown that the phase and group velocity of light along the x-direction in vacuum are:

$$v_{ph,x}^{Yee} = c \left[1 - \frac{1}{3} \left(1 - \frac{c\Delta t}{\Delta x} \right) \left(\frac{k_L \Delta x}{2} \right)^2 \right]$$

$$v_{g,x}^{Yee} = c \left[1 - \left(1 - \frac{c\Delta t}{\Delta x} \right) \left(\frac{k_L \Delta x}{2} \right)^2 \right]$$

where k_L is the wave number of the laser field. Due to requirements imposed by numerical stability, described in Section 3.2.2, $c\Delta t < \Delta x$. Therefore, $v_{ph,x}$ and $v_{g,x}$ will always be different from c, while it should be exactly c. When choosing the discretization of the grid, it is important to ensure that these numerical artefacts in the physical properties are small compared to the physical effects. For example, one should ensure that $c - v_{g,x}^{Yee} \ll c - v_g$, where v_g is the group velocity in the plasma. If this condition is not fulfilled, it will directly affect the dephasing length of the electron beam in the simulation since it depends on v_g. This may have implications on the injection of electrons at the back of the plasma wave, since the wave will travel at the phase velocity of the plasma wave, which is equal to the group velocity of the laser pulse. A reduction in the phase velocity of the plasma wave will increase the injection rate of electrons.

Lehe's numerical-Cherenkov-free solver

The discretization above imposes a sub-luminal speed of light. For relativistic electrons, this gives rise to a numerical artefact in the form of Cherenkov radiation. Phys-

Table 3.2: Tabulated values of α_m required to calculate the Courant–Friedrichs–Lewy (CFL) condition for Lehe's Maxwell solver. M is the highest mode used in the simulation.

M	0	1	2	3	4	5
α_M	0.210486	0.591305	3.5234	8.51041	15.5059	24.5037

ical Cherenkov radiation will be emitted when a charged particle travels faster than the phase velocity of light in the medium. In a plasma, the refractive index, η, < 1, which means that the phase velocity is super-luminal, therefore no Cherenkov radiation should be produced. However, since $v_{ph,x}^{Yee} < c$, it is possible for $v_{particle} > v_{ph,x}^{Yee}$ which, if true, will produce artificial Cherenkov radiation. This numerical Cherenkov radiation is a strong source of noise that will affect the electrons and degrade the emittance of the electron beam.

A solution to this problem has been proposed, by modifying the Yee scheme to introduce a small increase in the phase velocity in vacuum rather than a small decrease [45]. The scheme is modified in such a way that:

$$\delta_x = -\frac{1}{4}\left[\frac{\Delta x^2}{c^2\Delta t^2}\sin\left(\frac{\pi c\Delta t}{2\Delta x}\right)^2 - 1\right], \quad \beta_{\theta,x} = \beta_{r,x} = \frac{1}{4}. \tag{3.6}$$

which leads to the velocities

$$v_{ph,x}^{Lehe} = c\left[1 + \frac{2}{3}\left(1 - \frac{c\Delta t}{\Delta x}\right)\left(\frac{k_L\Delta x}{2}\right)^2\right]$$

$$v_{g,x}^{Lehe} = c\left[1 + 2\left(1 - \frac{c\Delta t}{\Delta x}\right)\left(\frac{k_L\Delta x}{2}\right)^2\right].$$

This scheme has been used during the work presented in this thesis.

3.2.2 The Courant–Friedrichs–Lewy condition

In order for the numerical solver to converge, it must fulfil the Courant–Friedrichs–Lewy (CFL) condition [46]. For the Yee solver used in CALDER-Circ, the CFL condition states:

$$c\Delta t < \left(\sqrt{\frac{1}{\Delta x^2} + \frac{1+\alpha_M}{\Delta r^2}}\right)^{-1} \tag{3.7}$$

where values of α_M are tabulated in Table 3.2.

If the numerical Cherenkov-free solver is used instead, the CFL condition is instead:

$$c\Delta t < \Delta x. \tag{3.8}$$

In the simulations, the boundary conditions imposes a more strict CFL condition, which is closer to the adapted Yee scheme.

For the Lehe solver, when $\Delta t \to \Delta x$, a strong metastable mode is excited on the grid. This mode does not grow exponentially, but can be rather strong, and if it appears it can be filtered. The mode is excited at the so-called Nyquist frequency, which is the highest frequency a grid with a spacing of Δx can resolve. This noise can therefore be effectively filtered out using a low-pass filter.

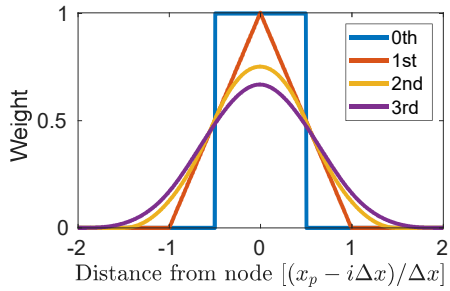

Figure 3.3: Different interpolation orders for the shape function. The 1st order is the convolution of the 0th order with itself. The 2nd order is the convolution of the 1st with the 0th, and so on. In this 1D example, x_p represents particle position, and X_j is the position.

3.2.3 Interpolation order

The grid and the macro-particles are coupled through a shape function, S, such that, for a macro-particle located on a grid at position $\mathbf{r_p}$, the grid value, F, at this position is calculated through the sum over the grid nodes, j:

$$F_p = F(\mathbf{r_p}) = \sum_j F_j S(\mathbf{r_p} - \mathbf{R_j}). \tag{3.9}$$

Examples of 1D shape functions are shown in Figure 3.3. Here, the S functions are defined as $S_0 = \theta(x + \Delta x/2) - \theta(x - \Delta x/2)$, where θ is the Heaviside function. The k:th order shape function is $S_k = S_{k-1} * S_0$, where $*$ is the convolution operator.

The 0th order function corresponds to the nearest grid point method, which simply applies the field value at the nearest grid point to the macro-particle. This is a very noisy method and is rarely used. First-order interpolation dramatically reduces the noise, and is piecewise continuous. Second-order interpolation further reduces the noise, since not only is the function continuous but its derivative is also continuous.

The benefit of increasing the interpolation order is that it reduces the numerical noise by smoothly coupling neighbouring grid points together. Noise can also be reduced by increasing the number of macro-particles, N, which is a statistical property, reducing the noise by a factor $1/\sqrt{N}$. The choice of interpolation order and the number of macro-particles is ultimately a trade-off between computational noise and computational cost. In most cases, the cost of increasing the interpolation order is less than that of increasing the number of particles[6]. Certain physical effects might be more sensitive to noise than others, it is therefore important to check the convergence of the simulations parameters before reaching conclusions, as is discussed in Section 5.7.

3.2.4 Particle pusher

The particle pusher implemented in CALDER-Circ is called the Boris pusher after its inventor [47]. Boris himself referred to it by a more descriptive name: the "half E" pusher. Calculating the new normalized momentum $\mathbf{u} = \gamma\mathbf{v}$, $\mathbf{u}$, $\mathbf{u}^{(n+\frac{1}{2})\Delta t}$ at the end of the time step, from the old velocity $\mathbf{u}^{(n-\frac{1}{2})\Delta t}$, known at the beginning of the time step, is divided into three steps using the magnetic and electric field at the particle

[6]This discussion on noise assumes that a sufficient number of macro-particles is used to represent the distribution function. Thus, the number of particles cannot be decreased arbitrarily. Furthermore, increasing the interpolation order also reduces the "resolution" of the plasma, e.g. sharp gradients in the plasma will be smeared out.

position. This method ensures second-order accuracy in the calculation of the velocity and movement. $\mathbf{u}$ is updated by

$$\begin{aligned}
\mathbf{u}^- &= \mathbf{u}^{(n-\frac{1}{2})\Delta t} + \frac{q\Delta t \mathbf{E}^{n\Delta t}}{2m}, \\
\mathbf{u}' &= \mathbf{u}^- + \mathbf{u}^- \times \mathbf{t}^{n\Delta t}, \\
\mathbf{u}^+ &= \mathbf{u}^- + \mathbf{u}' \times \frac{2\mathbf{t}^{n\Delta t}}{1 + \mathbf{t}^{n\Delta t} \cdot \mathbf{t}^{n\Delta t}}, \\
\mathbf{u}^{(n+\frac{1}{2})\Delta t} &= \mathbf{u}^+ + \frac{q\Delta t \mathbf{E}^{n\Delta t}}{2m}
\end{aligned}$$

where $\mathbf{t}^{n\Delta t} = \hat{\mathbf{B}} \tan[q\Delta t B^{n\Delta t}/(2\gamma^{n\Delta t} m)]$. Note that while the field representation in CALDER-Circ is reduced to quasi-cylindrical, the particles in CALDER-Circ are fully kinetic in 6D.

Time interpolation of the magnetic field

Due to the construction of the Yee scheme, where the electric and magnetic fields are known at a different time to increase the accuracy of the numerical solver, when pushing the particle, the value of the magnetic field should be interpolated to the time at which the electric field is known.

In the pusher of CALDER-Circ, the standard method interpolating the the magnetic field known at time steps $n \pm \frac{1}{2}$ to time step n is:

$$B_n = \frac{(B_{n-\Delta t/2} + B_{n+\Delta t/2})}{2} \tag{3.10}$$

However, for a relativistic electron co-propagating and overlapping a laser pulse, the error arising from this interpolation can be greater than the physical contribution to the force on the particle from the $(\mathbf{E} + \mathbf{v} \times \mathbf{B})$ in a laser field when the force from $\mathbf{E}$ and $\mathbf{v} \times \mathbf{B}$ have almost the same amplitude and are acting in opposite directions and thus largely compensate each other. Hence, a small error when calculating $\mathbf{v} \times \mathbf{B}$ can become of the same order as $(E_y - v_x B_z)$. This problem can be mitigated by expanding the interpolation to include earlier time steps, as implemeted in CALDER-Circ and described previously [48]. This is important when the laser pulse overlaps with the electron bunch, as discussed in Section 5.7.

3.2.5 Integrating current

To advance Maxwell's equations, the current density, $\mathbf{J}$, and charge density, ρ, must be calculated on the grid, from the statistical weight, W_p, the charge, Q_p, and the velocity, $\mathbf{v}_p$, are known for the macro-particles. A straightforward way of doing this is to calculate $\mathbf{J}_p = W_p Q_p \mathbf{v}_p / V$, where V is the cell volume. The macro-particle charge, Q_p, is projected onto the grid in a similar way as the fields are interpolated to the particle, instead, the values $\tilde{J}_x, \tilde{J}_r, \tilde{J}_\theta$ and $\tilde{\rho}$ are represented by F_p and deposited on the grid through

$$F_j = F(\mathbf{R_j}) = \sum_p F_p S(\mathbf{R_j} - \mathbf{r_p}). \tag{3.11}$$

Calculating the current density in this way introduces a small error, and the continuity equation is broken such that:

$$\frac{\partial \rho}{\partial t} + \nabla \mathbf{J} \neq 0 \tag{3.12}$$

and consequently Gauss's law becomes $\nabla \mathbf{E} = \rho + \epsilon$, where ϵ represents a small error. Therefore, another method is used to calculate the current density, by solving for $\mathbf{J}$ in the continuity equation is used. $\partial\rho/\partial t$ can be calculated on the grid and the gradient operator ∇ can be inverted using a method proposed by Esirkepov [49]. This method satisfies the continuity equation by definition and Gauss's law is therefore fulfilled. The Esirkepov algorithm was used for all simulations with CALDER-Circ presented in this thesis.

3.2.6 Ionization

An ionization module was used in CALDER-Circ to model the physics of the target containing nitrogen molecules (Papers II and VI). The module has been described in detail previously [50]. It is based on the Ammosov–Delone–Krainov (ADK) model for ionization [51], and takes into account multiple ionization levels in one time step. In these simulations, the nitrogen was assumed to be pre-ionized up to N^{5+}, so that only ionization close to the peak of the laser pulse is modelled, the outer electrons are assumed to be ionized by the leading edge of the laser pulse.

3.2.7 Boundary conditions

Boundary conditions must be applied to both fields and particles in PIC codes. These have different properties, for example, reflective or absorbing. Boundary conditions should be chosen with care to ensure that the physics that is simulated is not affected by unphysical phenomena that can occur at the boundaries.

In the simulations presented in this thesis, the upper and lower boundary in the x direction were absorbing. For the outer boundary in r, both reflective and absorbing boundaries were used for the electromagnetic fields. All boundaries were absorbing for the particles.

3.3 Calculating synchrotron radiation

In order to retrieve synchrotron radiation from CALDER-Circ, a post-processing code is used that calculates the emission radiated by the macro-particle trajectories, by evaluating either Equation (2.19) to obtain the power or Equation (2.21) to obtain the angular and spectral distributions.

From the denominator in Equation (2.21), it is clear that the radiation increases with increasing $\boldsymbol{\beta}$ especially when it is aligned with $\mathbf{n}$. The highest contribution from the high-energy electrons will thus be obtained when $\boldsymbol{\beta} \approx 1$, and it is therefore only necessary to track particles with an energy above a certain value, which simplifies the selection process. Furthermore, for the photon energies of interest, usually in the range 1-20 keV, the time resolution, needed to discretize such short wavelengths is much finer than that of the simulation.

To estimate the sampling frequency required, we can consider that in order to numerically resolve a wave with a certain frequency, it must be sampled at at least

twice that frequency. This is called the Nyquist criterion. For the grid to resolve the wavelength of a 5 keV photon (0.25 nm), to fulfil the Nyquist criterion, the simulation time steps would have to be 3200 times smaller than those needed to resolve a 800 nm laser wavelength. However, to calculate the betatron radiation it is only necessary to resolve the betatron oscillations. Due to relativistic effects, the time step, dt, at which the electron motion must be sampled is given by:

$$dt = \frac{\gamma^2}{f_{limit}} \tag{3.13}$$

where f_{limit} is the upper frequency that can be resolved from an electron with a Lorentz factor of γ. The particle oscillates with the betatron frequency given in Equation (2.18).

For example: to resolve X-rays radiated at an energy of $\mathcal{E}_{photon} = 5$ keV, corresponding to $f_{limit} = h/\mathcal{E}_{photon} = 1.21 \cdot 10^{18}$ Hz, from a 100 MeV electron, corresponding to $\gamma = 196$, the time step needed to resolve this is 32 fs. This should be compared to the normal time step in a PIC simulation for an 800 nm laser, which is on the order of 0.3 fs.

Chapter 4

Experimental Tools

Most of the experiments performed as part of this work were conducted using the multi-terawatt laser at the Lund Laser Centre. One experiment was conducted using a more powerful laser system (VEGA-2), at the Spanish Center for Pulsed Lasers (CLPU) in Salamanca. Both lasers are based on chirped pulse amplification (CPA) [2], a technique for which Donna Strickland and Gérard Mourou were rewarded the Nobel Prize in Physics in 2018. The technique avoids damaging optics by reducing the intensity of the pulses during the amplification stage by stretching it in time. After amplification, the pulses are recompressed in time, allowing a very high peak power to be achieved.

These laser pulses can not only be focused to ultra-high intensities, but they are also capable of producing some of the shortest light pulses that can be created by man-kind. These unique properties require unique measurement techniques. In this chapter, the chirped pulse amplification laser system is presented, followed by examples and discussions concerning the measurement of physical properties in the lab.

4.1 The multi-terawatt laser at the Lund Laser Centre

The experiments described in Papers II, III, VI, VII, and VIII were performed using the multi-terawatt laser at the Lund Laser Centre. The system is based on titanium-doped sapphire and produces pulses with up to 1.4 J after compression centred at a wavelength of 805 nm. The pulse duration after compression can be reduced to 32 fs, resulting in a peak power of about 40 TW.

A detailed schematic of the laser system is shown in Figure 4.1. A short pulse (20 fs) is created in the mode-locked oscillator, shown in a) in the figure. The pulse is then stretched c) to reduce its intensity by several orders of magnitude before further amplification. This is achieved by separating the wavelengths in the pulse using a diffraction grating. Each wavelength is sent on its own path with a path length proportional to the wavelength. The pulse is then recombined in space. However, the pulse is stretched in time, since each wavelength is delayed by a different amount of time. Each temporal position in the pulse now corresponds to a certain wavelength, and this is what is called a chirped pulse. The pulse is then further amplified in

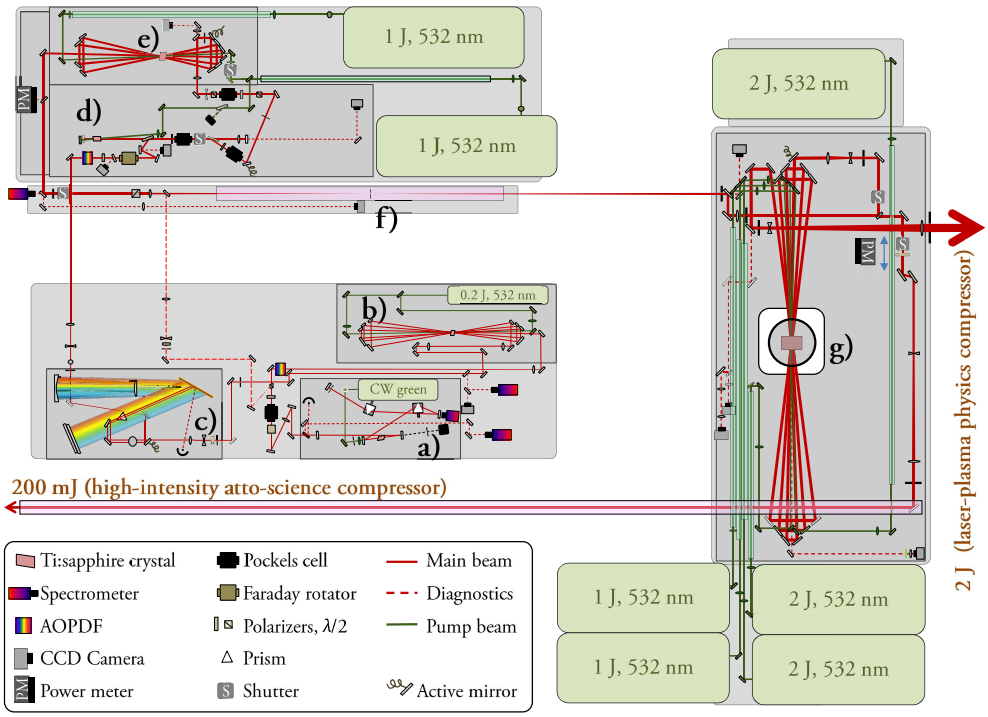

Figure 4.1: A detailed schematic of the multi-terawatt laser at the Lund Laser Centre. The beam is steered using active mirrors to keep the beam aligned throughout operation. a) A Kerr-lens mode-locked oscillator produces 80 million pulses per second with a duration of 20 fs. Every second, 10 pulses are selected to match the repetition rate of the pump lasers. Each pulse is sent to a pre-amplifier b) where the energy is increased from nJ- to µJ. The pulse is then stretched in time to around 450 ps in an Offner triplet stretcher, shown in c). The beam diameter is increased to 1.2 mm to match the cavity mode in the regenerative amplifier, shown in d), where the energy is amplified from µJ to mJ. The pulse is coupled out after 10 round trips, the beam diameter is increased to 9 mm and sent into a multi-pass amplifier (e) where the pulse is amplified to 0.4 J. The pulse then passes through a spatial filter, (f) and is split equally into two arms. In the high-power arm, the beam size is increased to 25 mm pulse and is then passes through the final amplifier (g) and the energy is increased by a factor 10, to 2J. The beam is then expanded to 60 mm and sent through the compressor in vacuum, with an optimal transmission of 70 %, where the beam is compressed to 35 fs. The phase-front of the beam is corrected using a deformable mirror, before it is sent to the experimental chambers. Figure courtesy of Isabel Gallardo González.

d) and e), and reaches the final amplification stage in g). The final amplification crystal is cooled to -180° C to increase the thermal conductivity of the crystal and thereby minimize the optical effects arising from thermal lensing. Before being sent to the experimental chamber, the laser pulse is recompressed in time. Recompression is achieved using the same principle as in the stretcher, but inverted. Furthermore, the pre-amplifier in b) is used to increase the temporal contrast of the laser system by reducing the amplification factor needed in the regenerative amplifier, where the

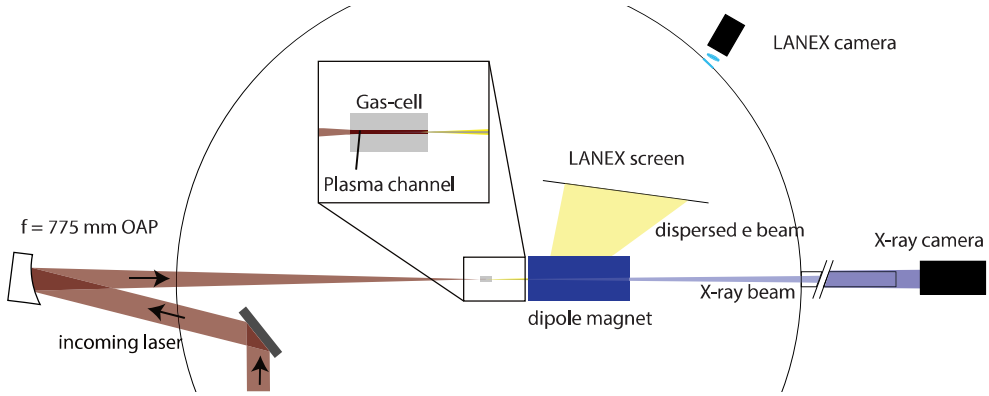

Figure 4.2: An example of an experimental setup. The laser pulse (brown) is sent to an off-axis parabolic (OAP) mirror that focuses the beam. A gas target is placed in the beam focus, and is ionized by the laser beam forming a plasma. This initiates a plasma wave that accelerates the electrons. The electrons are then dispersed by a dipole magnet onto a scintillation screen (LANEX), that is imaged by a camera. The electron spectrum can be retrieved from this image. An X-ray-sensitive camera is placed in the path of the X-rays produced. The data from the X-ray camera can be used either for X-ray imaging or to characterize the source.

majority of the amplified spontaneous emission in the system is created and pre-pulses are amplified.

4.2 Experimental diagnostics

A typical experimental setup is illustrated in Figure 4.2. The laser pulse is focused onto a gas target, creating a plasma. The peak of the laser pulse drives a plasma wave that accelerates electrons, which in turn produce X-rays. The electrons are sent through a 0.8 T, 200 mm long dipole magnet which disperses them according to their energy. The electrons then impinge on a scintillation screen that is imaged by a camera to retrieve the electron spectrum. Another camera is used to observe the X-rays travelling in the same direction as the focused laser pulse. The camera in this setup is used for single photon counting.

4.2.1 Laser diagnostics

Several methods of laser diagnostics can be used to characterize the laser pulse used in the experiment. During experiments, the pulse length is measured using a single-shot second-order auto-correlator [52]. Auto-correlator measurements are based on frequency doubling of the laser light in a 100 µm thick KDP crystal. The laser pulse is split into two parts, both of which are sent to the KDP crystal at different angles, creating a frequency-doubled signal in the direction of the bisector angle when the pulses overlap in time.

The spatial intensity profile of the second-order harmonic beam in the crystal will thus be the convolution of the temporal profile of the beam with itself. The method does not reveal the temporal pulse shape, and is therefore dependant on the choice

of pulse shape. For example, the sech^2 pulse shape produced in the oscillator and a Gaussian pulse have a very similar auto-correlator trace but for slightly different pulse durations.

$$\Delta\tau_{Auto}^{FWHM} = 1.54\Delta\tau_{sech^2}^{FWHM} = 1.41\Delta\tau_{Gauss}^{FWHM}.$$

The difference between the two pulse shapes in the most recent measurements performed at Lund Laser Centre is 33 fs if a sech^2 pulse is assumed, and 36 fs for a Gaussian. In the experiments presented in this thesis, the difference between the pulse shapes was between 37 and 40 fs. An example of a measurement using the autocorrelator is shown in Figure 4.3a) for the two different assumptions above. This small temporal difference was important to correctly reproduce the experimental results presented in Paper VI.

The pulse spectrum is measured at several locations in the laser chain, and can be tuned by adjusting a slit in the oscillator cavity or by tuning the transmission through a Dazzler. The pulse spectrum before the final amplifier in the laser room is shown in Figure 4.3b), where it can be seen that it is centred at 805 nm and the width is 38 nm (FWHM).

A commercially available third-order scanning autocorrelator (SEQUOIA) is used to measure the temporal contrast of the laser pulse. The third-order autocorrelator does not achieve the same time resolution as the second-order, but has a much higher dynamic range, they are therefore good complements to each other when characterizing the laser pulse. Figure 4.3c) shows the results of a measurement made with the laser system described above with the final amplifier turned off. In the figure, the intensity on the y-axis is based on the assumption that the temporal contrast is the same for full power pulse and that the focusability of the pre-pulse is the same as that of the main beam. The OTBI-levels for hydrogen, helium and some nitrogen ions are shown to emphasize that they may be ionized picoseconds before the main laser pulse arrives, validating the assumption that the main pulse interacts with a plasma.

A strongly attenuated image of the focal spot is optimized using an iterative algorithm with a feedback loop between a deformable mirror placed directly after the compressor and a phase-front sensor. The focus is usually optimized on a daily basis during experiments. An image of the focus is shown in Figure 4.3d). To calculate the intensity shown in the figure, a measured transmission of 60 % was assumed to be focused into the area shown in the figure, and that all the energy was located in a 35 fs temporal Gaussian pulse. Under these assumptions, a peak intensity of $9.0 \cdot 10^{18}$ W/cm^2 was calculated, which corresponds to $a_0 = 1.63$.

4.2.2 Electron diagnostics

During the work presented in this thesis, two types of diagnostics were used to characterize the electron bunches produced: measurements of the electron beam profile and measurement of the electron spectrum. The total charge of the electron beam can be estimated from the image of the electron beam on the scintillation screen captured by the camera. The response of the scintillation screen to the electron beam must be calibrated and the full optical efficiency of the complete imaging setup must be carefully analysed [53, 54].

To measure the electron spectrum, the electron bunch is sent through a dipole magnet, in which the electron beam is deflected by the Lorentz force. Since the velocity

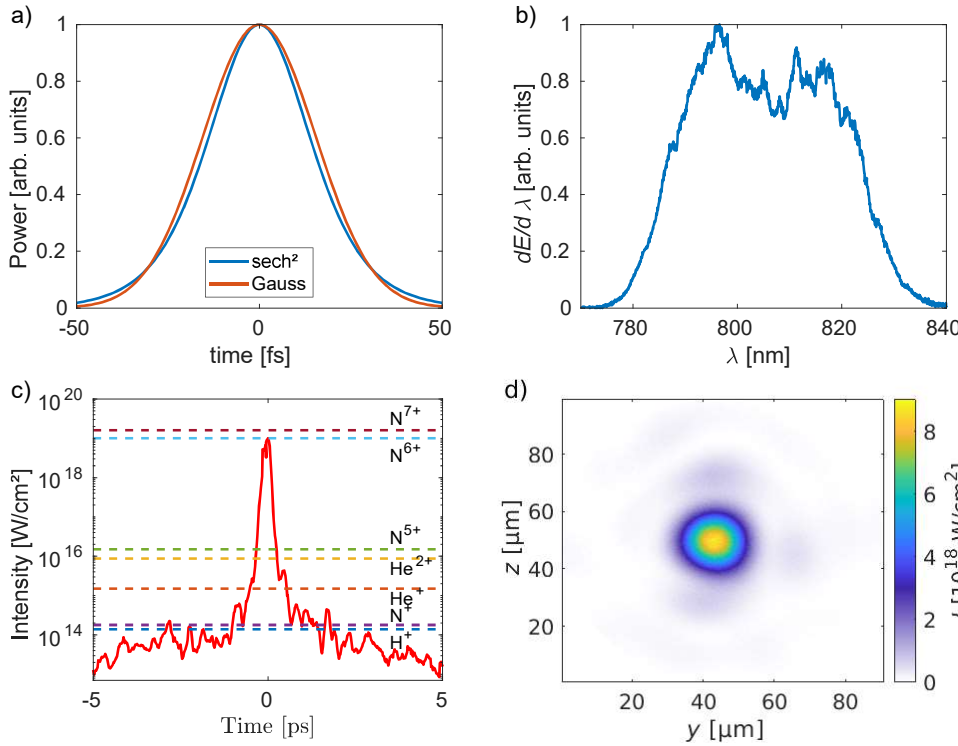

Figure 4.3: Laser pulse diagnostics. a) The signal interpreted from the autocorrelator for an assumed 33 fs sech^2 and a 36 fs Gaussian pulses. b) The spectrum of the laser pulse before the final amplifier. c) The laser contrast compared to different ionisation intensities as in Figure 2.1. Note that the timescale here is ps not fs. As can be seen, the laser can be expected to fully ionize a hydrogen atom already 1 ps before the main pulse, thus validating the assumption that the main pulse interacts with a plasma as is assumed in the simulations. d) An image of the laser focus with a FWHM spot size of 14 μm. The colour scale shows the estimated intensity assuming a 35 fs Gaussian pulse.

difference between the electrons is very small, and they all carry the same charge, they will be dispersed depending on their relativistic energy. The higher the kinetic energy of the electron, the less its trajectory will change. The bunch will therefore be dispersed according to their energy. After being dispersed, the electrons impinge on a scintillation screen, allowing the electron spectrum, charge and divergence to be retrieved. An example image of a dispersed electron beam is shown in Figure 4.4a). The data have been converted into angular and linear energy spectrum in 4.4b), while an integrated energy spectrum is shown in 4.4c).

Different dipole magnets were used in the different experiments. A 100 mm long, 0.7 T magnet was used for the experimental studies presented in Papers II, III, and VI. A 100 mm long, 1.2 T magnet was used for the study presented in Paper V. A 200 mm long, 0.8 T magnet was used for the experiments described in Papers VII, VIII and the study in Section 5.8. The longer magnet gives a better energy resolution for higher energies, and helps reducing the bremsstrahlung noise from the electrons

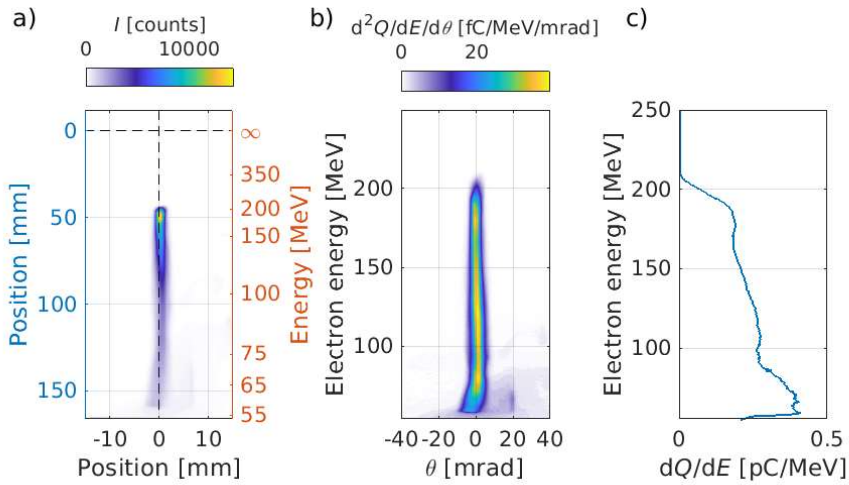

Figure 4.4: a) Raw data from the intensity image of the light emitted from the scintillating screen. The left axis gives the distance in mm from the optical axis, and the one on the right axis shows the corresponding electron energy. The optical axis hits the scintillator plane where the dashed lines cross. b) Raw data converted to a linearized spectrum and angular distribution of the electrons. c) The energy spectrum of the electron bunch integrated over the angular coordinate.

on the X-ray detector.

4.2.3 X-ray characterization by single-photon counting

As mentioned in Chapter 2, the wakefield acceleration process produces a synchrotron-like, femtosecond X-ray pulse with an energy in the keV range. It is of interest to characterize the X-ray spectrum for potential applications. X-rays can be detected indirectly, for example, using a scintillating material that absorbs X-rays and emits light in the visible spectrum, which is then imaged. However, X-rays with photon energies < 30 keV can be detected directly using, for example, a charged-coupled device (CCD). Direct detection is a feasible option for the laser wakefield accelerator at the Lund Laser Centre, which produce X-ray pulses with energies of a few keV. A CCD camera chip can be used for imaging, as described in Paper VIII, or to characterize the X-ray spectrum using a Ross filter [55, 56], or as a single-photon detector [57].

For an X-ray to be detected in the CCD chip the photon energy must be absorbed in the sensitive layer of the chip. When an X-ray photon is absorbed, it creates an ion-photoelectron, both of which further ionize surrounding atoms. The photoelectron starts a chain reaction that creates a µm-sized electron cloud in the sensor. The probability of an X-ray photon being absorbed in the CCD chip is called the quantum efficiency (QE), and is shown in Figure 4.5a). Some of the electrons produced in the CCD by the X-rays will end up in the conductor band of the semiconductor, which can be read out with the help of an applied voltage. In fact, there are many processes that deposits the photon energy in different ways. Most of the energy will generate heat in the detector, while more rare events, such as secondary X-rays, can lead to

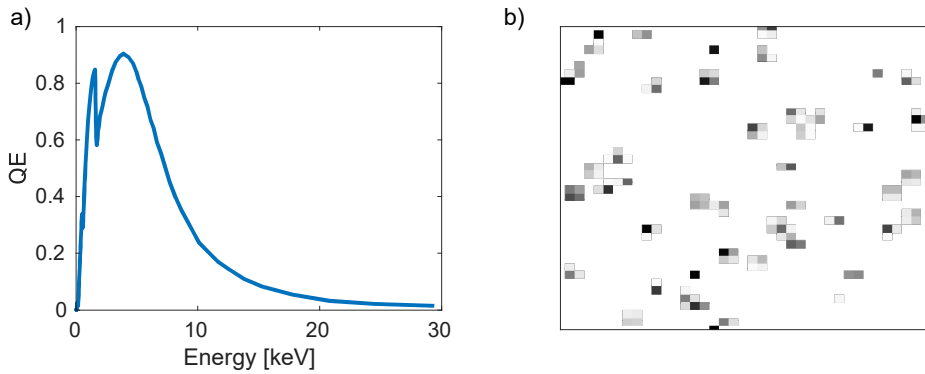

Figure 4.5: a) The quantum efficiency for the used CCD Camera. b) Example of single-photon counting signal in the CCD. The picture shows a distribution of 1-, 2-, 3-, and 4-pixel events as well as clustered events too large to origin from a single photon.

energy being deposited in other parts of the detector or being lost. The measured CCD signal (i.e. that arising from electrons in the conduction band) is proportional to the photon energy. However, the resolution is fundamentally limited by the Fano process [58], which is determined by the stochastic process that decides whether the electron ends up in the conduction band or is deposited as heat. The CCD detector can thus be used as a calorimeter, to measure the energy deposited by the X-ray photons. The signal from a CCD-detector is often referred to as analogue to digital (AD) units, which converts a number of electrons, to a discrete number of counts.

In a regime where only one photon hits the region of one pixel, the signal distribution over the pixels can be used to retrieve the spectrum. Each photon detected is referred to as an event. In reality however, the electron cloud might spread over several pixels, depending on the size of the cloud and the pixel size. An example of the event distribution over the CCD is shown in Figure 4.5b).

The energy resolution achievable, expressed as the FWHM, and denoted ΔE, depends on the electronic noise in the CCD chip N_{CCD}, the X-ray photon energy $\mathcal{E}_X$, the conversion from X-ray energy to electrons k_{eV2e} and the Fano factor F_X. The energy resolution can be calculated as [59]:

$$\Delta E = 2.355 k_{eV2e} \sqrt{N_{CCD}^2 + \frac{F_X \mathcal{E}_X}{k_{eV2e}}}. \tag{4.1}$$

For silicon, $k_{eV2e} = 3.6$ eV/electron [59], the Fano-factor is $F_X = 0.115$ [60]. The Fano noise sets a lower limit on the resolution, even if the electronic noise is eliminated. Note that for silicon, the Fano-process, with $F_X = 0.115$, increases the possible resolution compared to a pure Poisson distribution.

During the experiment presented in Paper VIII and the unpublished results presented in Section 5.8, the X-ray camera used was an iKon-L SO from Andor Technology with a back-illuminated deep-depletion chip. It has 2048 × 2048 pixels, and each pixel measures 13.5 µm × 13.5 µm. It can be cooled to a temperature of −70°C. The analogue-to-digital (AD) converter is 16 bits while the electron well depth over readout noise is closer to 15 bit.

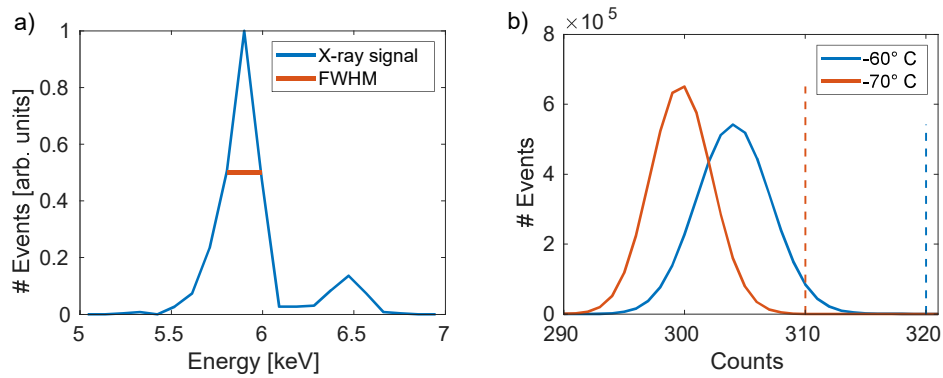

Figure 4.6: a) The energy spectrum for the radioactive isotope ^{55}Fe. The main peak is a combination of the K-α-1 peak (at 5.89875 keV) and the K-α-2 peak (at 5.88765 keV) X-rays. The smaller peak is the K-β peak at 6.49045 keV. This spectrum can be used to map the cameras AD-unit to energy. b) A histogram-like plot showing the number of pixels registering a certain count for a dark background image, integrated over 30 s at two different chip temperatures. It can be seen that reducing the lower temperature from -60°C to -70°C reduces the noise. The dashed vertical lines represent the pixel value over which 0.05 % of the pixels are located. The camera has a 16 bit AD converter, thus the maximum pixel value is 65535.

To convert the analogue signal to digital units recorded by the sensor, to photon energy, the sensor must be calibrated. The signal produced by the camera is measured so-called analogue to digital (AD) units. In Figure 4.6a), a known X-ray source was placed in front of the detector, and the spectrum was used to calibrate the relation between photon energy and AD-units. For the silicon chip used to collect the data presented in Section 5.8, the Fano limit was 109 eV. Figure 4.6a) shows calibration using a radioactive ^{55}Fe source. The measured FWHM is 188 eV. The readout noise from the detector at two different working temperatures, for an acquisition time of 30 s, is shown in Figure 4.6b).

An algorithm is needed to retrieve the spectrum from the raw data presented in Figure 4.5b). An event refers to a region of pixels that are direct neighbours, with a maximum size of 2×2 pixels if it should be considered a single photon event. The single-photon counting (SPC) algorithm consisted of the following steps: Detection of isolated events using threshold values. Discarding of events involving too many pixels. Integration of the pixel values for each event and conversion to photon energy using a calibrated value. Plotting a histogram of photon energies. A discussion of these steps is presented below.

A threshold value must be set to define an event, otherwise the noise from the sensor will be detected as events. This threshold can be determined by analysing the background signal. Figure 4.6b) shows background and noise data collected with the CCD at two different temperatures. The dashed vertical lines correspond to the 3-sigma value, a suitable threshold value for event-detection. If the threshold is set too low, single-pixel events will be interpreted as multi-pixel events, and the corresponding energy will be upshifted. If the threshold is set too high, two-pixel events may be interpreted as a single-pixel events, and the energy will be down-shifted in the

spectrum.

The events recorded in the detector must be categorized depending on whether an event is detected in one pixel, or if two, three or four neighbouring pixels are activated. These can then be classified as 1-, 2-, 3- or 4-pixel events. Note that only certain types of 3- and 4-pixel events are possible outcomes of a single-photon event. Three-pixel events must form a 90 degree angle, and 4-pixel events must form a square, otherwise they cannot originate from a single photon. The likelihood of detecting these different kinds of events will be determined by the size of the electron cloud produced by each absorbed X-ray photon. The electron cloud size specified for the iKon-L SO camera is sub-μm at 5 keV. From the distribution of pixel events recorded during calibration, the electron cloud seems to be closer to the size of a pixel than the specified value, as the distribution between the different pixel events is almost equal.

Chapter 5

Studies of Wakefield Acceleration

The work presented in this chapter can be divided into three closely related topics. The first is controlled trapping of plasma electrons in the accelerating wakefield. Trapping is the process by which background plasma electrons start to co-propagate with the plasma wave, and can be significantly accelerated. Trapping of electrons is important because it defines the initial bunch properties, and where acceleration starts, which has an impact on the final energy and the final bunch properties such as emittance, energy spread and bunch duration. For example, the energy stability of the electron bunch is sensitive to the trapping position in the plasma. If it varies by 100 μm, with field strengths on the order of 100 MV/mm, the final energy may differ by 10 MeV from shot-to-shot. As is mentioned in Chapter 2, there are different ways of achieving this. Three such methods were investigated experimentally and by simulations, as presented in Papers I, II and III.

The second topic concerns methods of achieving higher electron bunch energies. While the accelerating fields generated in a plasma can be several orders of magnitude stronger than in conventional accelerators, laser wakefield accelerators are currently limited by the length over which they can accelerate electrons. Two such limits are *diffraction* and *depletion* of the laser pulse itself. The laser will only remain focused and have sufficient intensity to efficiently excite a wakefield over a limited distance.

Diffraction can be compensated for by guiding techniques, while depletion requires some way of replacing the driver. A new concept for creating a guiding structure is described in Paper IV, while a means of injecting a new driver is discussed in Paper V.

Another limit results from *dephasing*, which arises when the highly relativistic electrons, travelling at a speed higher than that of the laser pulse in the plasma, catch up with the laser pulse, and thereby reach a decelerating phase of the plasma wave, where they cannot be accelerated further. One way to avoid dephasing is to use an electron bunch driver instead. The prospect of using an electron bunch from the linear accelerator at the MAX IV laboratory is discussed in this chapter.

The third topic is the important application of X-ray generation from the transverse oscillating motion of the electrons inside the accelerating structure, which pro-

duces synchrotron-like radiation with very short pulse durations and a small source size, allowing for applications such as X-ray spectroscopy with high temporal resolution. A method of enhancing these oscillations was investigated, and is described in this chapter and in Paper VI. Applications of this novel X-ray source in X-ray spectroscopy and in high-resolution X-ray imaging are demonstrated in Papers VII and VIII, respectively.

5.1 Controlled trapping in a density transition

To be able to adapt the wakefield accelerator to different applications, it is necessary to be able to control the properties of the electron bunch. Density down-ramp injection, as mentioned in Chapter 2, has the advantage of being well localized, thus providing a fixed starting point for the acceleration process. Furthermore, other properties of the electron bunch can be controlled by tuning the properties of the density down-ramp. In the transition from a higher density to a lower density, the plasma wavelength λ_p will increase, as it scales as $\lambda_p \propto 1/\sqrt{n_e}$. If trapping occurs during the full expansion of the bubble, the trapped charge will occupy the expanded region. It is therefore possible to control the electron bunch length by tuning the density difference between the two regions.

The amount of charge will increase if the expansion of the bubble is more rapid, for two main reasons. For a non-evolving driver, the plasma wavelength, and thus the bubble radius R, scales as $R \propto 1/\sqrt{n_e}$. In a linear density down-ramp, $n_e = n_0 - (dn/dx)x$, the change in radius is $dR/dx \propto (dn/dx)/(2n_e(x))^{3/2}$. For a steeper transition (larger dn/dx), the expansion will be faster. Two criteria must be fulfilled for the electron to be trapped: the electron must be located inside the bubble, and its velocity must be greater than that of the bubble back. While the bubble expands, a volume of electrons will be placed inside the bubble during expansion, and if the transition is steep enough, a number of electrons will also have a velocity greater than the velocity of the back of the bubble, v_{bb}, and can therefore be trapped. The bunch charge also depends on the length of the down-ramp, as a longer injection length results in more charge.

For a bubble that is expanding faster, the local velocity will decrease more, thus placing a larger volume of electrons inside the bubble, and lowering the velocity requirement in steep gradients for electrons to be trapped. The trapped electrons will have a larger spread both in initial position, r, and in radial momentum, p_r, which will lead to a higher emittance as defined in Section 2.3.6.

Paper I describes a study of the properties of the trapped electron bunch as a property of the density down-ramp. It is shown that the steepness (here characterized by dn/dx) and the density difference (between the regions before and after the density down-ramp) determines the amount of trapped charge, the electron bunch duration and the transverse emittance of the bunch. The key finding is that the parameters of the density down-ramp can be used to tune the properties of the electron bunch produced, and predictive models are presented for the amount of charge and the bunch duration.

The influence of the transition length was investigated for the case of very short to longer slow transitions and presented in Paper I. Figure 5.1a) shows the trapped charge per unit length of the ramp as a function of the transition steepness, which

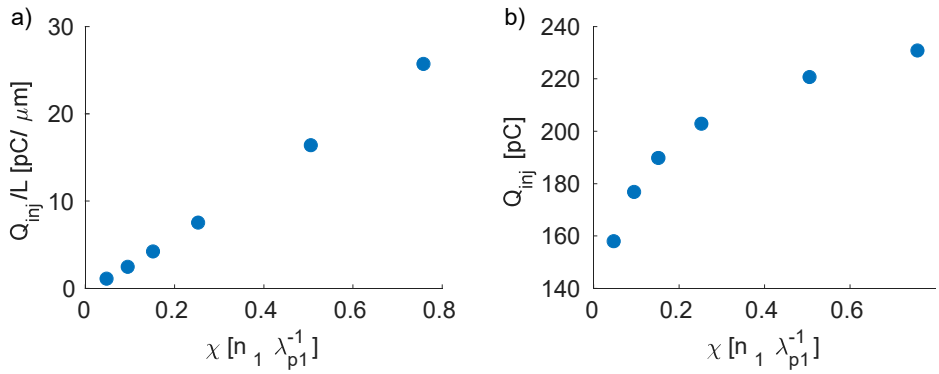

Figure 5.1: a) The charge over length of the down-ramp (Q/L) dependence on the density slope χ as presented in Paper I. b) The total charge (Q) for a fixed density transition as a function of the density slope.

can be compared with the total injected charge, shown in 5.1 b). χ is the the slope of the density gradient $-\partial n/\partial x$, expressed in units of the electron density at the upper plateau n_1 and the plasma wavelength λ_{p1} in the upper plateau. The amount of charge injected increases with an increasing gradient of the transition. The price of this, as can be seen in Figure 5 in Paper I, is an increase in the emittance of the electron bunch generated. On the other hand, an increase in charge and emittance is often desired when using the laser wakefield accelerator technique as a betatron X-ray source.

Figure 5.2 shows the initial positions of the trapped macro-particles initial positions in the plasma for two different down-ramp cases, obtained from simulations. The simulated laser pulse had a peak normalized vector potential of $a_0 = 1.8$ in a 18 µm focus in vacuum and the pulse duration was 30 fs. The pulse was sent into a plasma with an electron density of $n_1 = 6 \cdot 10^{18}$ cm^{-3}. The density later decreases in a density down-ramp. Two examples of the down-ramp are shown in Figure 5.2. The initial position of the particle is linked to the trajectory it will travel around the bubble. As can be seen for the long density down-ramp (the dashed red line) $\chi = 0.01$, the trajectory that is trapped starts at a transverse position, r_{ini}, which increases as the electron density decreases in the ramp. These macro-particles are trapped in the bubble very close to the center of the back of the bubble, as can be seen in Figure 6 d)-f) in Paper I. The spread in the radial position and momentum when the macro-particles are trapped is low, and yields a small emittance for the electron bunch. For the steep transition (solid blue line), $\chi = 0.76$, the spread in r_{ini} for each initial position along the propagation axis, x_{ini}, is significantly greater. This will correspond to a spread in the trapping position, r, and radial momentum, p_r. The consequence of this can be seen in Figure 6a)-c) in Paper I, where it is clear that the transverse size of the electron bunch is much larger than in the longer density down-ramp.

Note that the particles start their journey before the down-ramp. They are then pushed forward and sideways by the laser pulse, after which the laser pulse passes them, and they are accelerated backwards towards the center of the bubble. When the back of the bubble reaches the beginning of the density down-ramp, these electrons are positioned at the rear of the bubble, and are trapped during the expansion of the plasma wave.

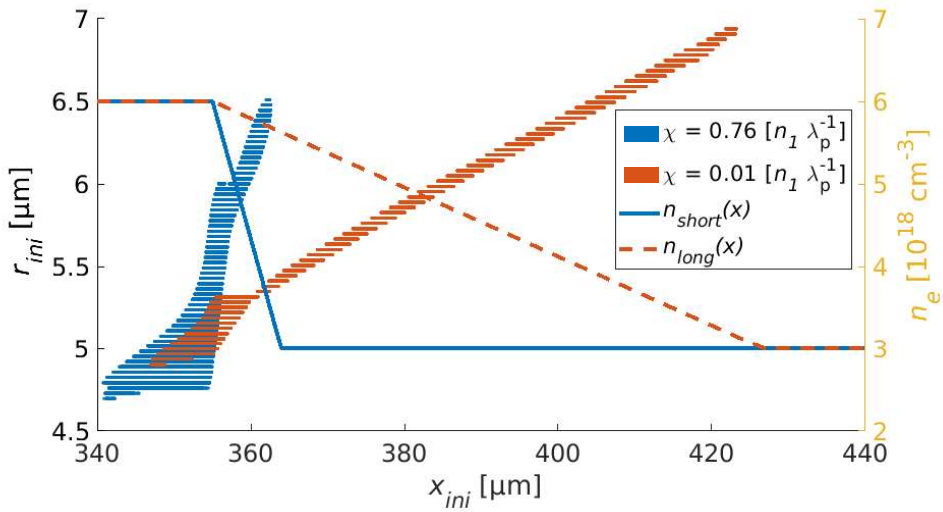

Figure 5.2: In the blue and red hatched regeions, the initial positions of the trapped macro-particles in the simulations for two different density slopes, shown as a solid blue line and a dashed red line with the density given shown on the right axis. The structured shape of the hatched region is due to the initialization pattern of the macro-particles in the code. The particle positions represented by red have been shifted half a discretization step to improve visibility. For the steeper tranistion, particles initiated further back and closer to the optical axis are trapped due to the more rapid expansion of the bubble.

As discussed in Paper I, at the beginning of the acceleration process, the electrons injected first will be more energetic than those that are trapped later. However, as acceleration proceeds, the electrons injected last will experience a stronger accelerating field. A designed gas target with a tailored density ramp can thus be tuned to minimize the energy spread of the electron bunch generated. This would be useful in applications requiring a low energy spread, for example, when a laser wakefield accelerator is used as an electron gun in a conventional electron accelerator or in next generation of accelerator-based free-electron lasers. The main purpose of such a gun would be to utilize the small normalized emittance of the electron beams produced in a plasma accelerator.

5.2 Localization of ionization-induced trapping

As is mentioned in Chapter 2, there are many ways to trap electrons. The trapping mechanism of choice will vary depending on the application. For the multi-terawatt laser in Lund, a density down-ramp has been shown to be a stable trapping process [61]. However, the amount of charge produced is relatively small. Using the same laser system, the charge can be increased by creating the electron bunch through ionization-induced trapping. Ionization-induced trapping typically creates an electron bunch with a continuous energy distribution. The bubble evolution in a density down-ramp will not only relax the trapping criteria for the electrons travelling along the bubble sheath, but will also influence the trapping condition of other trapping mechanisms.

Paper II describes locally enhanced injection from ionization-induced trapping in a density down-ramp, in such a way that the otherwise continuous ionization spectrum becomes peaked. The threshold for ionization-induced trapping was compared to the threshold for the self-trapping mechanism, and it was shown that ionization trapping starts at lower electron densities, and that in a certain density regime, at a fixed nitrogen concentration, the background electron density can be used to control the amount of charge. A regime was found where the bunch originating from ionization trapping could be combined with charge trapped from the background electrons in the density down-ramp at the exit of the gas cell. This created a pair of tightly spaced electron bunches separated in energy.

5.3 Colliding pulse injection

While trapping in a density down-ramp is a powerful way of localizing and controlling the electron bunch parameters, from an engineering point of view, it is difficult to create a very sharp small step in electron density. Such a transition is required to obtain a very narrow energy spread. Another way to achieve localized injection is by colliding a counter-propagating laser pulse with the wakefield driver. The beat wave caused by the interfering laser pulses will exert a ponderomotive force on the particles, which efficiently heats the electrons. This force can then push the electrons into a trajectory in the phase space such that they become trapped. Injection is then restricted to the location where the pulses collide. The strength of the beat wave, and by extension the amount of charge trapped, can be tuned by rotating the polarization of the injection pulse.

A compact colliding pulse experiment is described in Paper III. A small pick-up mirror was used to extract the injection pulse from the main driver pulse. Electron beams with a peaked spectrum and an energy spread of a few percent were produced. The effective accelerating field in the plasma was measured and found to be 90 MV/mm. The charge could be tuned by rotating the polarization, and the final energy could be tuned by moving the collision point, along the propagation direction of the main laser pulse, of the two laser pulses in the gas jet.

Simulations were performed to provide insight into the physics of the colliding pulse injection experiment. The simulations were performed at a collision angle of 180° using the quasi-cylindrical code CALDER-Circ. The simulation was successful in recreating the colliding pulse injection. The pulses had a FWHM duration of 37 fs, the driver pulse had a peak normalized vector potential of 1.1 in vacuum, and the injection pulse had a normalized vector potential of 0.3. The simulations were performed in an electron background density of $8 \cdot 10^{18}$ cm^{-3}.

Figure 5.3a)-c) shows three snapshots from a simulation around the event of colliding pulse trapping. The colour map shows the electron distribution in longitudinal phase space. The red line represents the electric field of the laser. In 5.3a) the counter-propagating, weaker pulse enters from right, and travels in the negative x-direction. In 5.3b) the counter-propagating pulse is close to the peak of the laser pulse driving a wakefield; the peak laser field for this time step is lower than in a) and c) due to the interference with the other pulse. In 5.3c) the counter-propagating pulse leaves the simulation box on the left. Electrons gain energy in the x-p_x space, as the counter-propagating pulse passes the wakefield. 5.3d) shows the x-p_x space at a later point

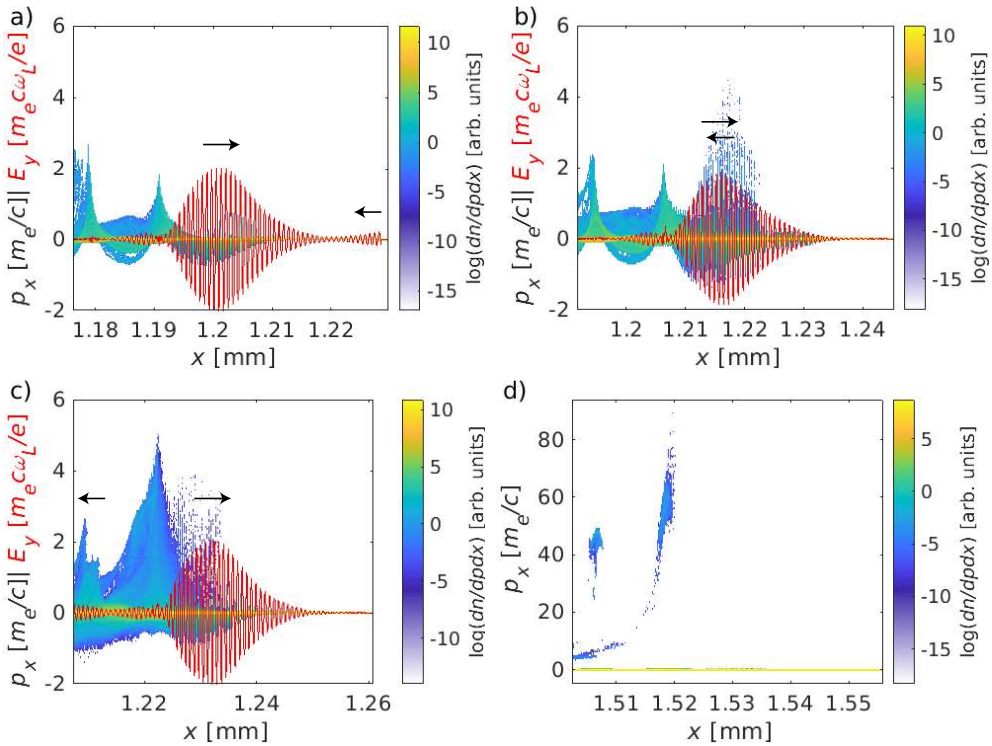

Figure 5.3: a), b), and c) show the phase-space distribution of electrons in x-p_x in color scale. In red is the laser field component E_y. The position and propagation direction of the two laser pulses are indicated with the black arrows. In a) the colliding pulse can be seen entering the box from the right. In b) the laser pulses interfere, heating the electrons. In c) the counter propagating laser pulse can be seen leaving the simulation box to the left. In d) the phase-space distribution is shown at a later point, where two electron bunches can be seen.

during the simulation, where accelerated electron bunches have that were trapped by the collision event have emerged from the background plasma.

It is clear from these simulations that trapping under these conditions is triggered by the colliding pulses. Two accelerated electron bunches were seen in the simulations (and perhaps more would have been visible if the simulation box had been larger). This agrees with experimental findings of the bunch structure [62].

5.4 An idea for a high-intensity optical guide

For a given laser system, parameters can be tuned, but the maximal power will be fixed. The maximal energy gain $\Delta\mathcal{E}$ in a wakefield accelerator with an external guide for the laser pulse scales more favourably for externally guided laser pulses than for completely self-guided pulses in the non-linear regime[20].

The ideal refractive index structure to guide a Gaussian laser pulse is a parabolic distribution in the radial direction, as is discussed in Paper IV. To guide a Gaussian

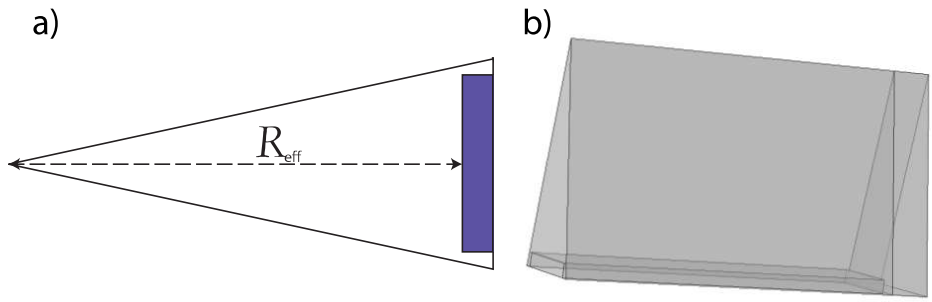

Figure 5.4: a) Schematic of a section of a polygon domain for the piezoelectric actuators (shown in blue). The effective radius R_{eff} which is used for the boundary condition to calculate the effective guiding channel is shown. b) The simulated volume in the commercial simulation program. The simulation utilizes 32-fold symmetry to make the simulation feasible. The rectangle at the bottom is the piezo volume, the triangular volume above is the fluid volume. The triangular volume at the end is a perfectly absorbing volume, simulating an infinite free space for the sound to leave the gas cell.

laser beam in a plasma, the spot size W should be matched to the plasma by $W = (r_m^2/(\pi r_e \Delta n_e))^{1/4}$, where $r_e = 2.818 \cdot 10^{-15}$ m is the classical electron radius, Δn_e is the difference in electron density between $r = 0$ and $r = r_m$. Thus it is the plasma density gradient $\partial n_e/\partial r$ that determines the guiding power of the a plasma channel.

To guide a laser pulse with a spot size $W_0 = 60$ µm in an on axis electron density of 10^{18} cm^{-3}, the density modulation from the background electron density should be increased 3 % over the distance $r_m = 60$ µm. In Paper IV a new type of gradient index optics structure was proposed for high intensity optics. The idea is to shape the plasma created by the laser pulse into a guiding structure by first shaping the unionized medium through a standing cylindrical sound wave. The gas medium used for laser wakefield acceleration is often hydrogen or helium due to their relatively low ionization threshold for complete ionization. At room temperature, the speed of sound in hydrogen is 1336 m/s and for helium it is 1007 m/s. To achieve sound wavelengths comparable to the laser spot size in helium, frequencies in the range of 1 MHz to 10 MHz are needed. Excitation of a radial mode using a cylindrical piezo actuator would be ideal, however, cylindrical piezo-actuators are not available at these frequencies. Therefore, an even-numbered polygon structure with flat actuators was designed, see Figure 1 in Paper IV. Acousto-fluid simulations were performed showing that it is feasible to achieve the required density modulation stronger than 3 % using piezo-actuators that can be produced today. A more detailed discussion of the implementation of such a device is given below, together with details on the acousto-fluid simulations performed to test the feasibility of the concept.

To excite the cylindrical standing wave in a regular polygon structure, the wavenumber of the acoustic wave, k_s is defined by R_{eff}, the distance from the center of the structure to the closest point of the actuator, as depicted in Figure 5.4a). Figure 5.4b) shows a 1/32 fraction of the simulation volume used in the acousto-fluid simulations. In the simulation 32-fold symmetry was used, greatly reducing the

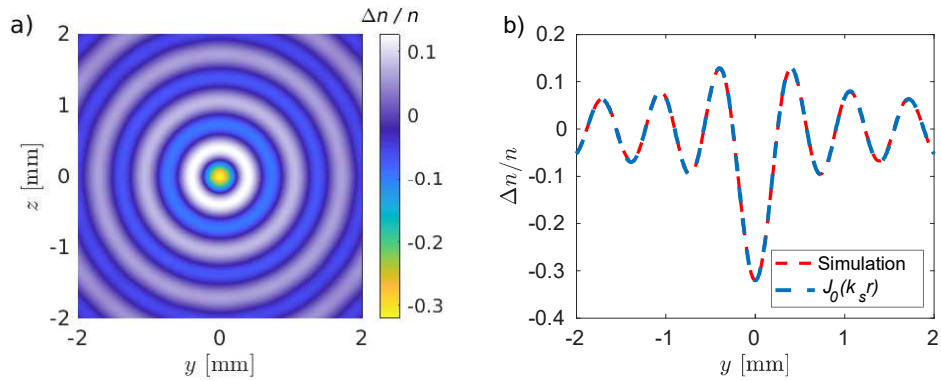

Figure 5.5: a) The excited standing wave pattern perpendicular to the laser propagation axis, in the center of a guide, containing hydrogen modelled as an ideal gas. b) A lineout from the results presented in a) compared to a Bessel function with the same peak value. As can be seen, a cylindrical wave is excited, and agrees with the analytical solution.

computer memory requirements.

The acousto-fluid simulations were performed using the ideal gas model. In the model, no losses except the sound waves leaving the simulation through the ends are taken into account. The driving frequency of the piezo-actuators in the simulations was matched to the radial cylindrical standing wave. The amplitude of the acoustic wave starts to be on the order of 10 %, even for rather modest amplitudes of the applied potential (e.g. 10 V peak-to-peak). A result from such a simulation is presented in Figure 5.5a). In b) the solution obtained is compared to the analytical solution to a cylindrical standing wave.

In the case of a laser wakefield accelerator, the gas cell would be placed in a vacuum chamber. Therefore, the gas cell would need to have walls with small apertures to allow the laser pulse to enter and exit the cell. The holes must be as small as possible to minimize the outflow of gas, increasing the pressure in the chamber. In the simplest case, the boundary conditions at the entrance and exit of the gas cell would be reflective walls instead of absorbing walls. In the simulations using the ideal gas model (i.e. no absorption) a longitudinal wave is excited, which is strong enough to modify the radial standing wave. The frequency response of a gas cell with absorbing walls is compared to the response of a system with reflective walls in Figure 5.6. Note that the system is sensitive to the excitation frequency, the amplitude of the frequency at 1 % frequency difference is 20 times less than at the resonance frequency. Figure 5.6b) shows the excitation of a longitudinal standing wave, modulating the longitudinal density profile.

In reality, no gas is ideal, and there will be losses in the gas medium that will end up as heat, even when using noble gases such as helium or argon. There will also be losses at the walls of the acoustic cavity, due to acoustic coupling to the radial walls. A linear solver can be used instead of the ideal gas model, and an attenuation coefficient can be added. The amplitude decreases with an increasing attenuation coefficient. At the same time the sensitivity to a slight frequency mismatch decreases and the longitudinal standing waves in the enclosed cell are suppressed.

Figure 5.7 shows a longer gas cell with multiple actuators, simulated to show the scalability in length of the proposed guide. The simulation results presented in

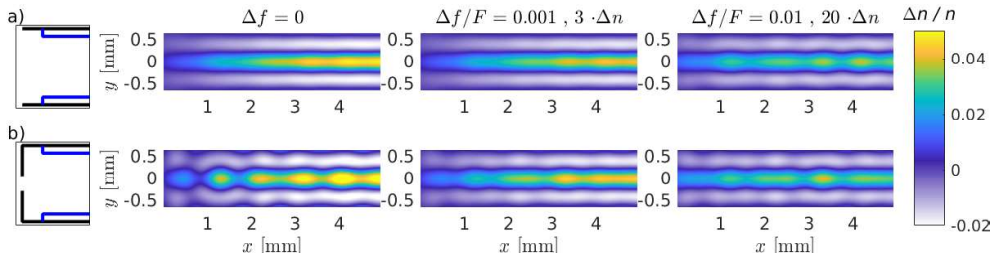

Figure 5.6: a) The frequency response using the ideal gas model for a guide with open (absorbing) ends. b) The results of a similar simulation using reflective walls, with only a small opening for sound to escape. The systems are sensitive to the applied piezo driver frequency, and when detuned by 1 %, the amplitude drops significantly. Note the modified amplitude above each column.

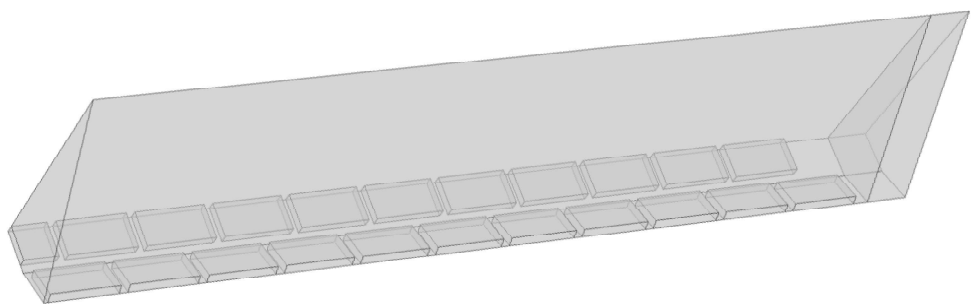

Figure 5.7: A model of a guide with many small piezo-actuators, designed to test the scalability of the proposed optical guide. Note how the piezo-actuators in the two different rows are shifted in longitudinal position to reduce longitudinal modulations in the standing acoustic wave produced. This model was used to obtain the results presented in Paper IV.

Paper IV are taken from a simulation performed with the model shown in Figure 5.7. The piezo-actuators were placed in a row along the propagation axis of the laser, and the piezo-actuators in the neighbouring rows are placed out of phase to minimize longitudinal density modulations arising from the longitudinal separation of the piezo-actuators.

5.5 Staging acceleration by merging laser wakefields

Although guiding techniques can be used to increase the maximum energy of the electrons, staging of laser wakefield accelerators will be needed to further accelerate the electrons, in order to reach energies interesting for future particle colliders in high-energy physics experiments. A proof-of-principle experiment on staging was recently performed at Lawrence Berkeley National Laboratory [63]. The wakefield accelerated electron bunch is produced in the first stage, refocused by an active plasma lens, and accelerated in the second stage. The second driver pulse is coupled in with a plasma mirror, through which the electron pulse must pass. An increase in energy is observed in the second stage, although other beam parameters are not preserved, which will be

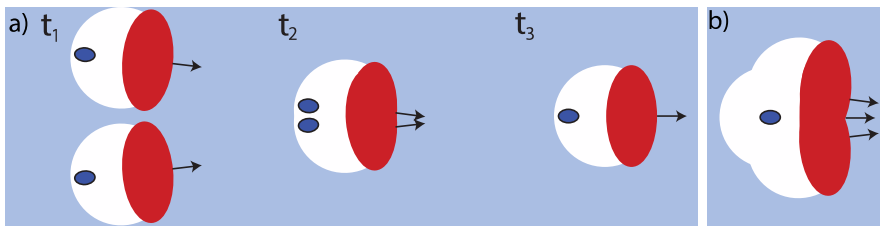

Figure 5.8: a) Before collision, at t_1, two laser wakefield drivers individually trap charge and accelerate charge. During collision, at t_2: The wakefields collide with charge that is already trapped. After collision, at t_3: one laser wakefield emerges, where the electrons from both bunches travel along the bisector angle. b) Collision in a hypothetical staging experiment by wakefield merging. The colliding wakefields in this picture do not accelerate their own electron beam, the driver of the first wakefield is almost completely depleted, and the electron bunch is almost dephased.

important in future accelerators.

Although the setup described above uses state-of-the-art compact plasma technologies, a draw-back is that the actual accelerating structure is short compared to the transportation line between the accelerating stages. One way to solve this, and better preserve the beam parameters, would be to remove the vacuum transportation segment between the acceleration stages. A solution has been proposed in which a curved plasma channel is used to guide a new driving pulse into the plasma [64]. Although this seems to be an interesting solution, the curved plasma channel itself has yet to be realized experimentally.

Paper V describes an experiment in which two laser driven wakefields were merged for the first time. Figure 5.8a) shows a conceptual illustration of the merging procedure. A 200 TW laser is split into two parts, and focused on a 5 mm long gas jet where the pulses collide. When the laser pulses are focused at a typical collision point of 0.4 mm inside the gas jet each pulse produces an electron bunch propagating in the direction of the individual laser pulse. However, when the laser pulses overlap in time and collide in the gas jet, only one electron bunch is accelerated in the direction in between the two individual laser pulses, called the bisector angle. This is a strong indication that the wakefields have been successfully merged into a single accelerating structure.

An alternative method of staging laser wakefield accelerators is also presented in Paper V, where the new driver pulse is injected by merging two laser pulses. This way, a new accelerating structure can be formed that is travelling in the same direction as the already produced electron bunch. A schematic showing merging in the case of staging is shown in Figure 5.8b). The new injected laser pulse has two purposes, to replenish the energy, and to rephase the electron bunch, both of which are necessary to ensure continued acceleration.

The merging of wakefields has previously been studied numerically [65–67] for other purposes. Perhaps the easiest way of imagining the merging of wakefields is perhaps to consider the refractive index created by the plasma wave in the blow-out regime, as is shown in Figure 2.6. If the angle is small enough, the optical structure of the bubbles can influence and bend the trajectory of both pulses, redirecting them in the bisector angle.

5.6 Towards a beam-driven wakefield accelerator at MAX IV

Another way to address the dephasing limit is to use a driver that propagates at the same speed as the witness bunch. This can be achieved using an electron driver bunch instead of a laser pulse [68]. As in the case of a laser driver, the electron bunch must be matched to the plasma to drive a wakefield efficiently. However, an electron bunch instead requires a bunch density higher than the surrounding plasma, and a bunch size on the order of a plasma wavelength in three dimensions. This requires a bunch with high current, a short duration, and low emittance, which few accelerators can deliver. One that can is the linear accelerator at the MAX IV laboratory.

The possibility of using the linear accelerator at the MAX IV laboratory, which is located in Lund, to perform wakefield acceleration experiments has been investigated. Particle tracking simulations of the accelerator show that it should be possible to produce an electron bunch with an electron density high enough to drive a non-linear plasma wakefield. Furthermore, the photocathode gun could be used to produce both a driver and a witness bunch [69, 70]. The driver bunch can be compressed to a few tens of fs, but the duration of the driver bunch and the distance between the two bunches are not independent, and in order to identify the parameters for wakefield acceleration, the background density must be chosen such that the bunch separation matches the non-linear plasma wavelength.

The electron bunches produced by the linear accelerator were found to be promising candidates for a witness-driver pair of electron bunches for a plasma wakefield accelerator using the CALDER-Circ code. Figure 5.9 shows a density map together with plots of the electric fields produced in a simulation. The electron density of the plasma is shown in blue, and the electron density of the electron bunches in copper.

The simulated driver bunch was 43 fs long (FWHM) and focused to a FWHM spot size of 10 μm. The witness bunch was 66 fs long, with the same focus size. The peak electron density is $6.0 \cdot 10^{17}$ cm^{-3} in the driver, and $2.6 \cdot 10^{17}$ cm^{-3} in the witness bunch. The bunches are separated by 194 fs. The background density of the plasma is $1.1 \cdot 10^{17}$ cm^{-3} with 0.5 mm linear transitions from vacuum to the peak density. The simulation was performed using the anti-Cherenkov scheme presented in Section 3.2.1 with a grid discretization of 0.255 μm in the x-direction and 0.51 μm in r. Two Fourier modes were used to represent the fields in the azimuthal direction. The simulation box was set to 183 μm × 51 μm.

As can be seen in Figure 5.9, the driver excites a bubble and can effectively accelerate a witness bunch. Figure 5.10 shows the results of acceleration, where it can be seen that the 100 pC witness bunch can be accelerated from 3 GeV to over 5 GeV. The 3 GeV driver bunch with a charge of 150 pC is efficiently depleted after 36 cm propagation in the plasma. Of the 0.45 J in the driver bunch at the start of the plasma, 0.2 J is transferred to the witness bunch, i.e. the efficiency is over 40 %.

Proton-driven wakefield acceleration of electrons was recently demonstrated at CERN, in the AWAKE [71] project. A beam-driven experiment called Flash Forward is currently underway at DESY in Hamburg, Germany [72] while FACET II at SLAC in Stanford, USA [73] will open for new experiments in 2020.

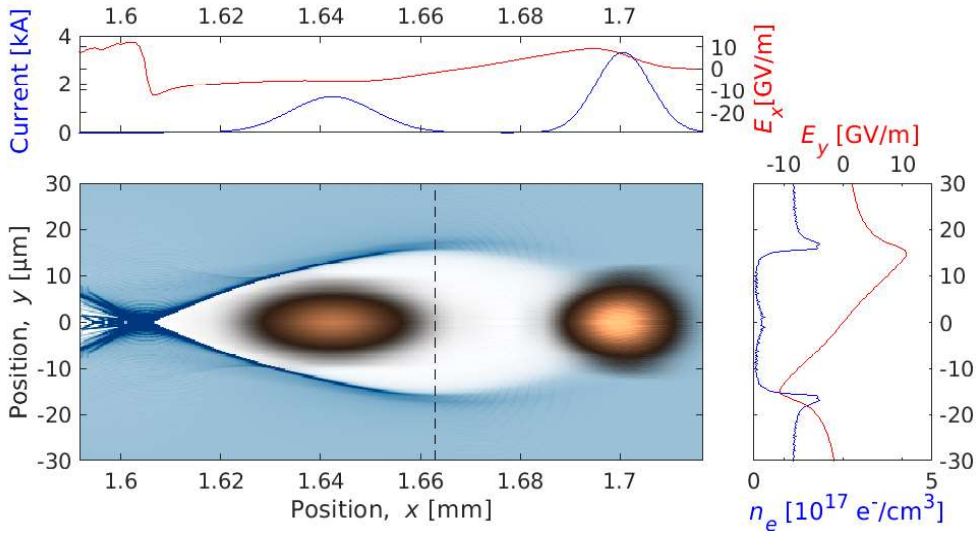

Figure 5.9: Results from simulations of beam parameters that should be achievable at the MAX IV linear accelerator. The driver and witness bunch are represented by the copper/black shaded regions: brighter regions corresponding to higher density. The background plasma density of electrons is shown in blue. Lighter colors correspond to lower density. The plot above the density map shows the longitudinal electric field E_x at $y = 0$ in red, and the current produces by the electron bunches along x in blue. For this configuration, an accelerating field of close to 6 GV/m is predicted for the witness bunch. The beam loading caused by the witness bunch flattens the accelerating field which reduces the increase in energy spread of the witness bunch. The plot on the right shows the focusing electric field E_y (red) and the electron density n_e (blue) along the dashed black line in the density map. Note that almost complete cavitation is achieved.

5.7 Direct laser acceleration

For a given laser system, the properties of the laser pulse are fixed, e.g. the highest possible pulse energy and the shortest pulse duration. Therefore, in many cases, the laser pulse will overlap the trapped electron beam. It is therefore interesting to study what effect this has on the electron bunch. The concept of direct laser acceleration (DLA) in an ion cavity was introduced in 1999 [74]. Here, the author described it as the inverse free-electron laser mechanism with the potential to accelerate electrons. In the same paper, a resonance condition for DLA

$$\frac{\omega_\beta}{\omega_L} = 1 - \frac{v_\parallel}{v_{ph}} \tag{5.1}$$

was defined, where ω_β is the betatron frequency defined in Section 2.4, ω_L is the laser frequency, $v_\parallel$ is the electron velocity in the propagation direction, and v_{ph} is the phase velocity of the laser. The betatron motion of the electron will be in resonance with the laser if the laser phase advances one full period during one full betatron oscillation. In this way, the electron can gain forward momentum from the laser, through the rotation of the transverse momentum into longitudinal momentum by the laser's magnetic field. As $v_{ph} > c$ in a plasma, and $\omega_\beta \propto \gamma^{-1}$, the resonance condition

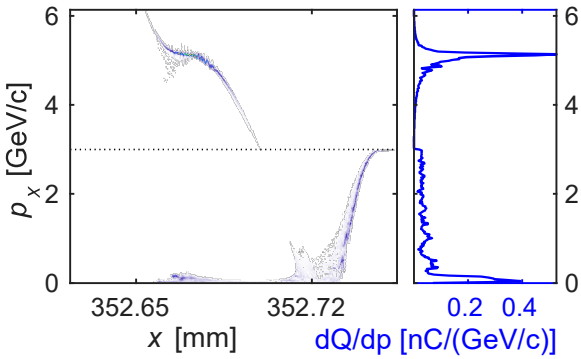

Figure 5.10: The x-p_x phase-space distribution of the driver and witness bunch at the end of the simulation. It can be seen that most of the driver's energy has been depleted while the main part of the witness bunch has been evenly accelerated to 5 GeV. The energy spectrum of the electrons is shown on the right. The witness bunch is clearly peaked with an energy spread of a few %.

will change as the electron is accelerated, it will therefore not stay in an accelerating phase.

DLA in wakefield acceleration can be tested by allowing the laser to overlap the injected electron bunch. This can be achieved by increasing the length of the laser pulse, such that it becomes comparable to the length of the bubble, or by increasing the background density, such that the bubble shrinks to the size of the laser pulse.

The effect of the dopant concentration (N_2 in a H_2 gas mixture) in ionization-induced trapping of electrons for different densities was investigated and is presented in Paper VI. It was found that as the density increased, the amount of accelerated charge increased, to a level where injection became saturated. If the molecular concentration of nitrogen was increased to 5 %, the beam loading arising from the injected electron bunch decreased the peak electron energy. Furthermore, at higher electron background densities and with higher concentrations of nitrogen, a forked structure is seen on the electron spectrometer, showing that the electrons with the highest energies have two preferential propagation directions. The forked structure seen in the present experiment has been observed in other experiments using similar laser parameters [75]. The forked structure is most visible at higher concentrations of nitrogen because there are more electrons injected in the region where the DLA effect is strong, thus a larger number of electrons is significantly accelerated by DLA, and beam loading reduces the energy of the electrons mainly accelerated by the wakefield. In fact, when the electron spectra shown in Figure 2 (a) in Paper VI are saturated to enhance the visibility of regions with low charge in the spectra, the DLA fork can be seen in all four spectra, indicating that the acceleration process is still acting, but fewer electrons are affected.

When trying to reproduce the experiment in simulations, the DLA effect was significantly stronger in the simulations than in the experiments. The modulations seen in the beam profile were strong. When performing a convergence test, it became clear that the properties of the electron bunch changed when the resolution of the simulation was increased. An error in the interpolation of the magnetic field in time numerically enhanced the DLA effect, as is discussed in Section 3.2.4. This error could be reduced when increasing the interpolation order in time.

To show that the artificial enhancement of the DLA effect is weaker than the physical effect, three simulations were performed and compared. The enhancement of the DLA effect is revealed by overly enhanced betatron oscillation, and it is therefore

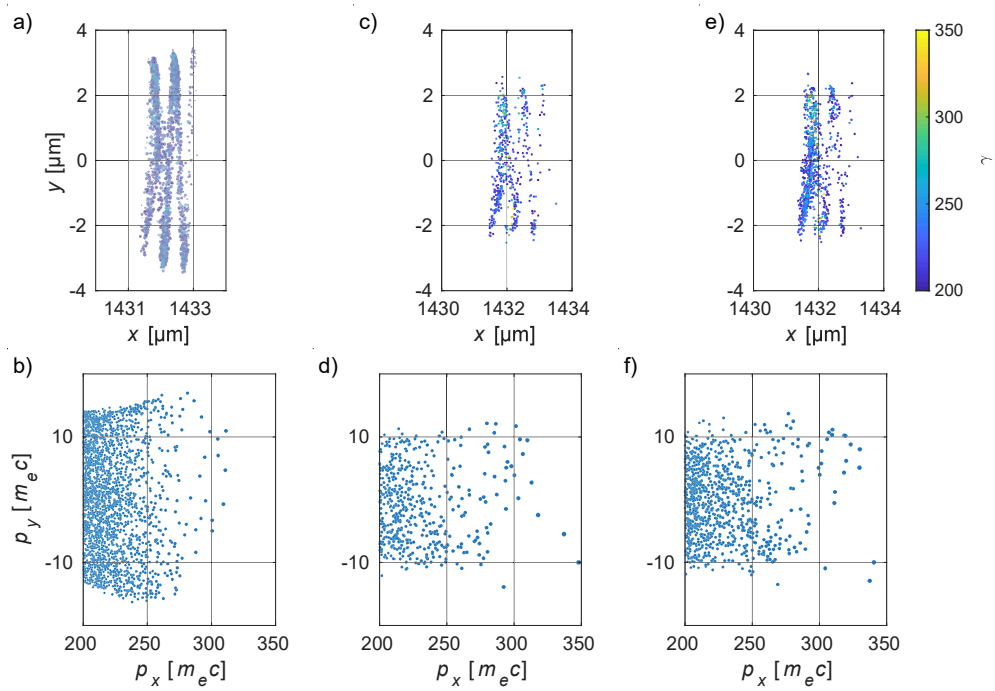

Figure 5.11: Results from a convergence test for DLA-simulations. The plots show the distribution of macro-particles with $\gamma > 200$ in x-y space (upper plots) and p_x-p_y space (lower plots) for three different simulation settings. In a) and b) a time-step of 52 as was used together with first-order interpolation in time for the magnetic field. In c) and d) a time-step of 52 as was used together with second-order interpolation in time for the magnetic field. In e) and f) a time-step of 26 as was used together with second-order interpolation in time for the magnetic field. The structure of the electron bunch in c) and e) is similar, while it differs significantly in transverse size compared to a).

interesting to study the distribution of the particles in the polarization direction of the laser (y) and the corresponding momentum (p_y). The simulation setup is identical to that presented in Paper VI, except for the laser pulse duration, which was changed to 40 fs, while maintaining the laser energy. Figure 5.11 shows the distribution of a randomly selected sample of macro-particles with $\gamma > 200$ from three different simulations at the same position in the plasma. In a) and b) the "standard" resolution which usually has converged was used to simulate laser wakefield acceleration. The results shown in c) and d) were run with the same resolution, but with second order interpolation in time, and e) and f) show results from a simulation run with twice the resolution of the electromagnetic grid, also using second-order interpolation in time. Note the distribution of the particles in the different plots. It can be seen that the beam is wider, both in y and p_y, in a) and b), than in the other two cases. The particles in c) and d) are distributed over the same region as the particles in e) and f).

The numerically enhanced DLA oscillations may lead to overestimated conclusions on effects such as micro-bunching of the electrons, enhanced X-ray generation, and

reduced average speed of the electrons. Nevertheless, the DLA effect is physical, and the X-ray generation will be affected, as discussed in the next section.

5.8 The DLA-enhanced X-ray source and its applications

Papers VII and VIII describe the use of a betatron X-ray source based on ionization-induced trapping in a 6 mm long gas cell. This X-ray source deliver a high stable flux compared to other methods tested at the Lund Laser Centre. It is important to note that the gas cell is operated at an electron density of 10^{19} cm^{-3} or above. The length of the gas cell is longer than both the depletion and dephasing length of the laser. An investigations of the effects of a focus with aberrations reported in the literature [76] show that it may take longer to form a bubble structure, thus delaying the acceleration process. Furthermore, if significant charge is generated, the acceleration process will transition into a beam-driven regime when the laser depletes, which will generate X-rays [77]. It can be argued that if only the betatron X-rays produced are to be used, as the absorption of X-rays in the under-dense plasma is low, adding a few millimeters of plasma to make sure the laser pulse is fully depleted will not have any deleterious effects.

An experiment was conducted to investigate the influence of the length of the plasma medium on the generated X-rays. The experimental setup is shown in Figure 4.2. The electron bunch produced was deflected onto a scintillating screen. The X-rays were sent to a 27.6 mm x 27.6 mm back-illuminated deep depletion CCD placed 4 m away from the source. The X-rays propagated through two 250 μm beryllium vacuum windows, an aluminium filter and 4 cm of air before reaching the CCD. The aluminium filter was a 2 x 2 matrix dividing the CCD sensor into 4 regions blocked by 0, 120, 240, and 480 μm of aluminium. This was done to cover a wider range of X-ray flux using the same experimental setup. The laser pulse energy was 750 mJ and the duration 37 fs, and was focused to a spot size of 14 μm.

Data were collected with four different gas cell lengths: 1.5, 4, 5, and 9 mm, and four different backing pressures, 0.2, 0.25, 0.3, and 0.35 bar. The gas used was a mixture of 99 % helium and 1 % nitrogen. Assuming a filling factor of 90 %, the backing pressure of 0.23 bar corresponds to an electron density of 10^{19} cm^{-3} for fully ionized helium. The results are presented in Figure 5.12. The total integrated signal on the CCD chip is shown in Figure 5.12a). While the optimized flux is similar for $L = 1.5$ mm and longer gas cell lengths, the longer cells porduce a more stable X-ray flux over a wider range of backing pressures. For the two shortest gas cell lengths, 1.5 mm and 3 mm, the flux increases up to a backing pressure of 0.3 bar, while for gas cell length longer than 3 mm, the flux reached a plateau above 0.25 and 0.3 bar. Note that for the 7 mm and 9 mm cells, the stability of the generated X-ray flux increases between 0.25 and 0.3 bars.

Figure 5.12b) shows the fitted critical energy to the data obtained using the single-photon counting algorithm and calibration described in Chapter 4. At 0.2 bar, the flux was too low to calculate a critical energy for the 1.5 mm and 3 mm gas cells. The general trend suggests that the critical energy increases up to a backing pressure of 0.3 bar. The non-linear plasma wavelength at $1.5 \cdot 10^{19}$ cm^{-3} is 8.6 μm, accounting for the scaling presented in Chapter 2, and the plasma wavelength for $a_0 \approx 2$ is 12 μm. This is very similar to the FWHM pulse length of the laser (11 μm), suggesting

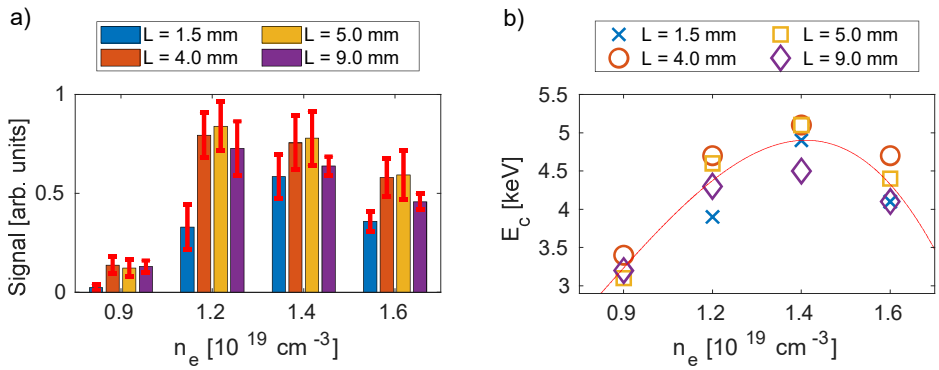

Figure 5.12: a) Total integrated signal on the X-ray camera chip for the different lengths at different pressures. Note how the b) Estimated critical energy E_c for the different lengths at different pressures.

that the critical energy is highest when the DLA effect on the electron is strongest.

To further investigate this effect, simulations were performed in CALDER-Circ. Two densities were studied, $1.0 \cdot 10^{19}$ cm^{-3} and $1.5 \cdot 10^{19}$ cm^{-3}. The code was modified to numerically cancel the DLA mechanism to investigate the influence of this mechanism has on the critical energy. To cancel out the interaction between the accelerated particles and the laser field, Fourier decomposition was used to cancel the interaction of macro-particles with a normalized forward momentum, $p_x < 40$ with the mode $m = 1$, which contains the linearly polarized laser fields. A 2.5 mm density plateau, with 0.55 mm long density ramps at the entrance and exit, was simulated.

The critical energy obtained with and without the DLA effect for the lower density case was 4.6 and 3.9 keV, respectively. For the higher density the critical energy with DLA increased to 5.8 keV, and was reduced to 3.8 keV without the DLA effect. In relation to the experimental data, we note that the critical energy increases with the density, while for the case with the DLA effect artificially cancelled, the critical energy is similar for both cases.

The study described above thus showed that using a longer gas cell created an X-ray source that is less sensitive to variations in the background density. Furthermore, there is a peak in the critical energy of the X-rays when the laser pulse length is similar to the size of the plasma bubble. This X-ray source was used in the studies presented in Papers VII and VIII. The source size was larger in the polarization direction of the laser (VIII), supporting the influence of DLA on the electron bunch.

Chapter 6

Summary and Outlook

The work presented in this thesis has contributed mainly to three important aspects of wakefield accelerators and their applications: *controlled trapping*, *increased energies* and *X-ray emission and applications*. Three different trapping methods were studied in simulations. A numerical study showed that it is possible to tune the electron bunch properties using density down-ramp trapping. Clear relations between the down-ramp properties and the electron bunch properties were identified, and predictive models were constructed. To support and interpret experimental data, simulations were performed to mimic the acceleration process in the experiments. A type of electron spectrum with two energy peaks observed in experiments was identified as a combination of two different trapping mechanisms, ionization-induced injection and trapping in a density down-ramp, in simulations.

There are now many ways and ideas to create electron bunches from the background plasma in wakefield accelerators. As the technology advances, higher demands are placed on the produced electron bunches. While the community has an understanding of localized injection and how to create certain kinds of electron bunches, there will eventually be demands on creating polarized electron beams for a future collider. An important part of trapping is the stability of the laser pulse itself, and the fluctuations in the laser pulse will put a limit on how stable the accelerator can be, therefore large efforts have to be put into developing the laser systems, for these accelerators to become commercial products. Electron bunches created from the background plasma are very compact, compared to most conventional sources. This is due to the small size of the accelerating structure, which makes laser wakefield accelerators suitable as electron sources for high brightness beams at accelerator facilities.

On the topic of *increased energies* several different studies were performed. First, a novel way to create plasma structures for optical guiding, using ultra-sound to modify the gas density was suggested. The original idea was developed into a model, and commercial engineering software was used to test the feasibility of the concept. Extensive simulations were performed using data for materials commercially available, and a prototype was designed. Second, an experiment on merging two laser wakefield structures was designed and performed at an external laser facility. The main objective of the experiment, to show that wakefields can be merged, was demonstrated. This successful experiment led to a novel concept to stage laser wakefield accelerators

without a need for intermediate electron optics was developed based on the possibility to merge laser wakefield structures. Third, plasma simulations were performed to investigate the possibility of using electron bunches from the linear accelerator at the MAX IV laboratory in a proposed future wakefield acceleration experiment. A regime where almost complete cavitation was achieved and an accelerating field of 6 GV/m was found. The input parameters for the simulation were based on simulations performed of the actual linear accelerator.

A future high-energy collider based on plasma technology is an ambitious goal. While single-stage plasma-based electron accelerators is a maturing technology, the activity on positron accelerators around the world is very low. Ultimately a positron accelerator will be needed, before a collider can be built. The next step towards a collider experiment based on electron beam driven technology, is to show that electron bunch parameters can be preserved during acceleration in the plasma wave. For laser wakefield accelerators, staging has to be achieved without ruining the bunch parameters. These tasks should not be impossible, but very challenging, which makes me unsure of the time-scale to be expected for these challenges to be overcome. However, similar challenges have been faced by pioneers in other fields of research, that are standard technology today.

On *X-ray emission and applications*, many simulations were performed to reproduce the experimental results that identified the direct laser acceleration process. The method was tested, and the physics of direct laser acceleration in a laser wakefield accelerator could be investigated. A separate experiment characterizing and investigating a laser wakefield acceleration-based X-ray source was designed and performed, and supported by simulations, identifying three processes that affect the X-ray generation in the laser wakefield accelerator. The betatron oscillations in a laser wakefield accelerator, the driven direct laser acceleration oscillation process, and the transition into a beam-driven regime that decelerates the electron bunch again. A single-photon counting setup was designed and characterized as a diagnostic for this experiment. Finally, two different experiments were performed using this X-ray source to perform X-ray spectroscopy and to do phase-contrast imaging, demonstrating the applicability of the technique.

The wakefield accelerator as an X-ray source is the most applicable use of these kind of accelerators today. While there is plenty of room for further improvements, they are already competitive for certain applications, given the compact setup and the precise synchronization with high-power laser pulses. In my mind, these X-ray sources could very well be made available in university labs around the world as dedicated intense and ultra-short-pulse X-ray sources, and not only as side activities in wakefield acceleration research laboratories.

The author's contribution

For all articles, the author has read and reviewed the manuscript. All the simulations were performed by the author using the PIC-code CALDER-Circ for Papers I, II, VI, as well as supporting simulations not presented in the final paper for Paper III. The author has participated in the maintenance and operation of the laser for Papers VII and VIII.

I **A tunable electron beam source using trapping of electrons in a density down-ramp in laser wakefield acceleration**
The author took an active part in the planning and the design of the study. The author performed all the simulations, analyzed and interpreted the data and wrote the manuscript with the help and input from the co-authors.

II **Localization of ionization-induced trapping in a laser wakefield accelerator using a density down-ramp**
The author performed all the simulations to reproduce the experimental results, supported the interpretation and analysis of the simulations, and actively discussed the results and gave input on the manuscript. The experiment was performed before the author joined the group.

III **Injection of electrons by colliding laser pulses in a laser wakefield accelerator**
The author performed simulations that were used in the discussion and development of the manuscript. The experiment was performed before the author joined the group.

IV **An acousto-optic waveguide for high-intensity lasers**
The author suggested the concept, performed all the simulations and wrote the manuscript with input from the co-authors.

V **Electron acceleration from merging laser wakefields**
The author took an active part in the planning of the experiment, especially the X-ray and Thomson-scattering diagnostics. The author also took an active part in performing the experimental campaign for the full duration. The author took an active part in discussing and developing the manuscript.

VI **Effects of the dopant concentration in laser wakefield and direct laser acceleration of electrons**
The author performed the simulations to reproduce the experimental data, analyzed and interpreted the simulation data together with the co-authors, and took an active part in the interpretation of the experimental results together with the co-authors. The experiment was performed before the author joined the group.

VII **Highly efficient angularly resolving X-ray spectrometer optimized for absorption measurements with collimated sources**
The author took an active part in preparing the experimental setup, including testing the X-ray source, and performing the experiment. The author also took part in the operation of the laser system.

VIII **Optimization of soft X-ray phase-contrast tomography using a laser wakefield accelerator**
The author took an active part in building and characterizing the experimental setup. The author supported the analysis of the experimental parameters, and took an active part in the discussion and development of the manuscript.

Acknowledgements

This thesis is based on work performed with colleagues from different parts of the world. This page is dedicated to the people who helped me complete the work presented here.

First and foremost, this would not have been possible without the guidance, and help from my supervisors. I would like to express my sincere gratitude to Olle Lundh who shaped this PhD project to combine my interests, for the free reigns and encouragement to pursue my ideas, and for the developing questions asked. To Claes-Göran Wahlström, for sparking the interest I have gained for this topic and for inviting me to the group. To Xavier Davoine, for always enthusiastically teaching me about physics and PIC codes.

To my colleagues who I had the pleasure to interact with on a daily basis, for interesting scientific discussions, many shared coffees, and for their support in various matters. In particular to the people with whom I worked closely with: To Martin for teaching me how to perform experiments, for his support, and his practical approach to physics. To Isabel, for sharing this adventure, for all the shared laser know-how, for the support, and for always smiling when saying hello. To Anders, for teaching me about the laser system and for always finding what is needed in the lab. To Jonas, for being great company during many trips and for maintaining the cake calendar. To Diego, for pushing new interesting projects and for uniting the group... tomorrow. To the people who's time in the group overlapped with mine and collectively built the experiments and kept the laser running: Kristoffer, Lovisa, Malay, Kristoffer, Alexander, Ylva, Giada, Jonathan, Jack, Philip, and Robin. To the people at the division of atomic physics I had the pleasure of meeting and conversing with. In particular to Anne, Jakob, and Åke for all the help regarding less scientific matters. To Lars Rippe for his support and discussion on my slightly off-topic project.

To all the involved in the Pliona project, for inspiring talks, ideas and conversations. To Julien for the extensive collaboration and to Arkady for the exchange of ideas and all the interesting discussions. To the team at CLPU in Salamanca for their hospitality. To Michal and Katerina for the interesting applications of this accelerator they made me aware of.

To my family and friends for their unrelenting support. To Ellen, for all the proof-reading, the graphical designs, for the patience, but most of all, for everything that matters.

References

1. T. Tajima and J. M. Dawson. *Laser electron accelerator.* Phys. Rev. Lett. **43**, 267 (1979).

2. D. Strickland and G. Mourou. *Compression of amplified chirped optical pulses.* Opt. Commun. **55**, 447–449 (1985).

3. S. P. D. Mangles, C. D. Murphy, Z. Najmudin, A. G. R. Thomas, J. L. Collier, A. E. Dangor, E. J. Divall, P. S. Foster, J. G. Gallacher, C. J. Hooker et al. *Monoenergetic beams of relativistic electrons from intense laser–plasma interactions.* Nature **431**, 535 (2004).

4. J. Faure, Y. Glinec, A. Pukhov, S. Kiselev, S. Gordienko, E. Lefebvre, J.-P. Rousseau, F. Burgy and V. Malka. *A laser–plasma accelerator producing monoenergetic electron beams.* Nature **431**, 541 (2004).

5. C. G. R. Geddes, C. S. Toth, J. Van Tilborg, E. Esarey, C. B. Schroeder, D. Bruhwiler, C. Nieter, J. Cary and W. P. Leemans. *High-quality electron beams from a laser wakefield accelerator using plasma-channel guiding.* Nature **431**, 538 (2004).

6. P. Gibbon. *Short pulse laser interactions with matter.* Imperial College Press (2005).

7. F. F. Chen. *Introduction to plasma physics.* Plenum Press 227 West 17th Street, New York, N.Y. 10011 (1976). ISBN 0306307553. Second printing.

8. B. Quesnel and P. Mora. *Theory and simulation of the interaction of ultraintense laser pulses with electrons in vacuum.* Phys. Rev. E **58**, 3719–3732 (1998).

9. T. J. Mehrling, R. A. Fonseca, A. Martinez de la Ossa and J. Vieira. *Mitigation of the hose instability in plasma-wakefield accelerators.* Phys. Rev. Lett. **118**, 174801 (2017).

10. E. Esarey, C. B. Schroeder and W. P. Leemans. *Physics of laser-driven plasma-based electron accelerators.* Rev. Mod. Phys. **81**, 1229–1285 (2009).

11. L. M. Gorbunov and V. I. Kirsanov. *Excitation of plasma waves by an electromagnetic wave packet.* J. Exp. Theor. Phys. **66**, 290 (1987).

12. P. Sprangle, E. Esarey, A. Ting and G. Joyce. *Laser wakefield acceleration and relativistic optical guiding.* Appl. Phys. Lett. **53**, 2146 (1988).

13. R. Lehe. *Improvement of laser-wakefield accelerators: towards a compact free electron laser.* PhD thesis (2014). 2014EPXX0058.

14. J. Faure. *Plasma injection schemes for laser-plasma accelerators.* CERN Yellow Reports **1**, 143 (2016).

15. A. Pukhov and J. Meyer-ter-Vehn. *Laser wake field acceleration: the highly non-linear broken-wave regime.* Appl. Phys. B **74**, 355–361 (2002).

16. J. B. Rosenzweig, B. Breizman, T. Katsouleas and J. J. Su. *Acceleration and focusing of electrons in two-dimensional nonlinear plasma wake fields.* Phys. Rev. A **44**, R6189–R6192 (1991).

17. E. Esarey, P. Sprangle, J. Krall and A. Ting. *Overview of plasma-based accelerator concepts.* IEEE Trans. Plasma Sci. **24**, 252–288 (1996).

18. G. Z. Sun, E. Ott, Y. C. Lee and P. Guzdar. *Self-focusing of short intense pulses in plasmas.* Phys. Fluids **30**, 526–532 (1987).

19. P. Sprangle, C.-M. Tang and E. Esarey. *Relativistic self-focusing of short-pulse radiation beams in plasmas.* IEEE Trans. Plasma Sci. **15**, 145–153 (1987).

20. W. Lu, M. Tzoufras, C. Joshi, F. S. Tsung, W. B. Mori, J. Vieira, R. A. Fonseca and L. O. Silva. *Generating multi-GeV electron bunches using single stage laser wakefield acceleration in a 3D nonlinear regime.* Phys. Rev. ST Accel. Beams **10**, 061301 (2007).

21. W. Lu, C. Huang, M. Zhou, M. Tzoufras, F. S. Tsung, W. B. Mori and T. Katsouleas. *A nonlinear theory for multidimensional relativistic plasma wave wakefields.* Phys. Plasmas **13**, 056709 (2006).

22. W. Lu, C. Huang, M. Zhou, W. B. Mori and T. Katsouleas. *Nonlinear theory for relativistic plasma wakefields in the blowout regime.* Phys. Rev. Lett. **96**, 165002 (2006).

23. S. Kalmykov, S. A. Yi, V. Khudik and G. Shvets. *Electron self-injection and trapping into an evolving plasma bubble.* Phys. Rev. Lett. **103**, 135004 (2009).

24. I. Kostyukov, E. Nerush, A. Pukhov and V. Seredov. *A multidimensional theory for electron trapping by a plasma wake generated in the bubble regime.* New J. Phys. **12**, 045009 (2010).

25. S. A. Yi, V. Khudik, S. Y. Kalmykov and G. Shvets. *Hamiltonian analysis of electron self-injection and acceleration into an evolving plasma bubble.* Plasma Phys. and Control. Fusion **53**, 014012 (2010).

26. S. Bulanov, N. Naumova, F. Pegoraro and J. Sakai. *Particle injection into the wave acceleration phase due to nonlinear wake wave breaking.* Phys. Rev. E **58**, R5257–R5260 (1998).

27. H. Suk, N. Barov, J. B. Rosenzweig and E. Esarey. *Plasma electron trapping and acceleration in a plasma wake field using a density transition.* Phys. Rev. Lett. **86**, 1011–1014 (2001).

28. A. G. R. Thomas. *Scalings for radiation from plasma bubbles.* Phys. Plasmas **17**, 056708 (2010).

29. M. Chen, Z.-M. Sheng, Y.-Y. Ma and J. Zhang. *Electron injection and trapping in a laser wakefield by field ionization to high-charge states of gases.* J. Appl. Phys. **99**, 056109 (2006).

30. A. Pak, K. A. Marsh, S. F. Martins, W. Lu, W. B. Mori and C. Joshi. *Injection and trapping of tunnel-ionized electrons into laser-produced wakes.* Phys. Rev. Lett. **104**, 025003 (2010).

31. D. Umstadter, J. K. Kim and E. Dodd. *Laser injection of ultrashort electron pulses into wakefield plasma waves.* Phys. Rev. Lett. **76**, 2073–2076 (1996).

32. E. Esarey, R. F. Hubbard, W. P. Leemans, A. Ting and P. Sprangle. *Electron injection into plasma wakefields by colliding laser pulses.* Phys. Rev. Lett. **79**, 2682–2685 (1997).

33. G. Fubiani, E. Esarey, C. B. Schroeder and W. P. Leemans. *Beat wave injection of electrons into plasma waves using two interfering laser pulses.* Phys. Rev. E **70**, 016402 (2004).

34. J. Faure, C. Rechatin, A. Norlin, A. Lifschitz, Y. Glinec and V. Malka. *Controlled injection and acceleration of electrons in plasma wakefields by colliding laser pulses.* Nature **444**, 737 (2006).

35. K. Floettmann. *Some basic features of the beam emittance.* Phys. Rev. Accel. Beams **6**, 034202 (2003).

36. E. Esarey, B. A. Shadwick, P. Catravas and W. P. Leemans. *Synchrotron radiation from electron beams in plasma-focusing channels.* Phys. Rev. E **65**, 056505 (2002).

37. S. Corde, K. Ta Phuoc, G. Lambert, R. Fitour, V. Malka, A. Rousse, A. Beck and E. Lefebvre. *Femtosecond x rays from laser-plasma accelerators.* Rev. Mod. Phys. **85**, 1–48 (2013).

38. J. D. Jackson. *Classical Electrodynamics.* John Wiley & Sons, Inc. 111 River Street, Hoboken, NJ 07030 3rd edition (1998). ISBN 09780471309321.

39. N. Bostrom. *Are we living in a computer simulation?* Philos Q. **53**, 243–255 (2003).

40. A. F. Lifschitz, X. Davoine, E. Lefebvre, J. Faure, C. Rechatin and V. Malka. *Particle-in-Cell modelling of laser-plasma interaction using Fourier decomposition.* J. Comput. Phys. **228**, 1803 (2009).

41. M. W. Evans, F. H. Harlow and E. Bromberg. *The particle-in-cell method for hydrodynamic calculations* (1957).

42. C. K. Birdsall and A. B. Langdon. *Plasma physics via computer simulation.* CRC press (2004).

43. C. K. Birdsall. *Particle-in-cell charged-particle simulations, plus Monte Carlo collisions with neutral atoms, PIC-MCC.* IEEE Trans. Plasma Sci. **19**, 65–85 (1991).

44. K. Yee. *Numerical solution of initial boundary value problems involving Maxwell's equations in isotropic media.* IEEE Trans. Antennas Propag. **14**, 302–307 (1966).

45. R. Lehe, A. Lifschitz, C. Thaury, V. Malka and X. Davoine. *Numerical growth of emittance in simulations of laser-wakefield acceleration.* Phys. Rev. ST Accel. Beams **16**, 021301 (2013).

46. R. Courant, K. Friedrichs and H. Lewy. *Über die partiellen Differenzengleichungen der mathematischen Physik.* Math. Ann. **100**, 32–74 (1928).

47. J. P. Boris. *Relativistic plasma simulation-optimization of a hybrid code.* Proceeding of Fourth Conference on Numerical Simulations of Plasmas (1970).

48. R. Lehe, C. Thaury, E. Guillaume, A. Lifschitz and V. Malka. *Laser-plasma lens for laser-wakefield accelerators.* Phys. Rev. ST Accel. Beams **17**, 121301 (2014).

49. T. Z. Esirkepov. *Exact charge conservation scheme for Particle-in-Cell simulation with an arbitrary form-factor.* Comput. Phys. Commun. **135**, 144–153 (2001).

50. R. Nuter, L. Gremillet, E. Lefebvre, A. Levy, T. Ceccotti and P. Martin. *Field ionization model implemented in Particle In Cell code and applied to laser-accelerated carbon ions.* Phys. Plasmas **18**, 033107 (2011).

51. M. V. Ammosov, N. B. Delone, V. Krainov, A. M. Perelomov, V. Popov, M. Terentev, G. L. Yudin and M. Y. Ivanov. *Tunnel ionization of complex atoms and of atomic ions in an alternating electric field.* Sov. Phys. JETP **64**, 1191–1194 (1986).

52. J. A. Armstrong. *Measurement of picosecond laser pulse widths.* Appl. Phys. Lett. **10**, 16–18 (1967).

53. A. Buck, K. Zeil, A. Popp, K. Schmid, A. Jochmann, S. D. Kraft, B. Hidding, T. Kudyakov, C. M. S. Sears, L. Veisz, S. Karsch, J. Pawelke, R. Sauerbrey, T. Cowan, F. Krausz and U. Schramm. *Absolute charge calibration of scintillating screens for relativistic electron detection.* Rev. Sci. Instrum. **81**, 033301 (2010).

54. Y. Glinec, J. Faure, A. Guemnie-Tafo, V. Malka, H. Monard, J. P. Larbre, V. De Waele, J. L. Marignier and M. Mostafavi. *Absolute calibration for a broad range single shot electron spectrometer.* Rev. Sci. Instrum. **77**, 103301 (2006).

55. P. Kirkpatrick. *On the theory and use of ross filters.* Rev. Sci. Instrum. **10**, 186–191 (1939).

56. P. Kirkpatrick. *Theory and use of ross filters. II.* Rev. Sci. Instrum. **15**, 223–229 (1944).

57. W. Fullagar, J. Uhlig, M. Walczak, S. Canton and V. Sundstöm. *The use and characterization of a backilluminated charge-coupled device in investigations of pulsed x-ray and radiation sources.* Rev. Sci. Instrum. **79**, 103302 (2008).

58. U. Fano. *Ionization yield of radiations. II. The fluctuations of the number of ions.* Phys. Rev. **72**, 26–29 (1947).

59. D. H. Lumb, G. D. Berthiaume, D. N. Burrows, G. P. Garmire and J. A. Nousek. *Charge coupled devices (CCDs) in X-ray astronomy.* Exp. Astron. **2**, 179–201 (1991).

60. R. C. Alig, S. Bloom and C. W. Struck. *Scattering by ionization and phonon emission in semiconductors.* Phys. Rev. B **22**, 5565–5582 (1980).

61. M. Hansson, B. Aurand, X. Davoine, H. Ekerfelt, K. Svensson, A. Persson, C.-G. Wahlström and O. Lundh. *Down-ramp injection and independently controlled acceleration of electrons in a tailored laser wakefield accelerator.* Phys. Rev. ST Accel. Beams **18**, 071303 (2015).

62. O. Lundh, C. Rechatin, J. Lim, V. Malka and J. Faure. *Experimental measurements of electron-bunch trains in a laser-plasma accelerator.* Phys. Rev. Lett. **110**, 065005 (2013).

63. S. Steinke, J. Van Tilborg, C. Benedetti, C. G. R. Geddes, C.B. Schroeder, J. Daniels, K. K. Swanson, A. J. Gonsalves, K. Nakamura, N. H. Matlis, B. H. Shaw, E. Esarey and W. P. Leemans. *Multistage coupling of independent laser-plasma accelerators.* Nature **530**, 190 (2016).

64. J. Luo, M. Chen, W. Y. Wu, S. M. Weng, Z. M. Sheng, C. B. Schroeder, D. A. Jaroszynski, E. Esarey, W. P. Leemans, W. B. Mori and J. Zhang. *Multistage cupling of laser-wakefield accelerators with curved plasma channels.* Phys. Rev. Lett. **120**, 154801 (2018).

65. M. Wen, B. Shen, X. Zhang, L. Ji, W. Wang, J. Xu and Y. Yu. *Generation of high charged energetic electrons by using multiparallel laser pulses.* Phys. Plasmas **17**, 103113 (2010).

66. L. Yang, Z. Deng, C. T. Zhou, M. Y. Yu and X. Wang. *High-charge energetic electron bunch generated by intersecting laser pulses.* Phys. Plasmas **20**, 033102 (2013).

67. E. Wallin, A. Gonoskov and M. Marklund. *Radiation emission from braided electrons in interacting wakefields.* Phys. Plasmas **24**, 093101 (2017).

68. P. Chen, J. M. Dawson, R. W. Huff and T. Katsouleas. *Acceleration of electrons by the interaction of a bunched electron beam with a plasma.* Phys. Rev. Lett. **54**, 693 (1985).

69. J. Björklund Svensson, F. Lindau, J. Andersson, M. Kotur, H. Ekerfelt, S. Werin, S. Thorin, O. Lundh, E. Mansten and F. Curbis. *Driver-witness-bunches for plasma-wakefield acceleration at the MAX IV linear accelerator* (2017).

70. J. Björklund Svensson, H. Ekerfelt, O. Lundh, E. Mansten, J. Andersson, M. Kotur, F. Lindau, S. Thorin and T. K. Charles. *Beamline design for plasma-wakefield acceleration experiments at MAX IV.* In *2018 IEEE Advanced Accelerator Concepts Workshop (AAC)* pages 1–4. IEEE (2018).

71. E. Gschwendtner, E. Adli, L. Amorim, R. Apsimon, R. Assmann, A.-M. Bachmann, F. Batsch, J. Bauche, V.K. Berglyd Olsen, M. Bernardini, R. Bingham, B. Biskup, T. Bohl, C. Bracco, P.N. Burrows, G. Burt, B. Buttenschön, A. Butterworth, A. Caldwell, M. Cascella, E. Chevallay, S. Cipiccia, H. Damerau, L. Deacon, P. Dirksen, S. Doebert, U. Dorda, J. Farmer, V. Fedosseev, E. Feldbaumer, R. Fiorito, R. Fonseca, F. Friebel, A.A. Gorn, O. Grulke, J. Hansen, C. Hessler, W. Hofle, J. Holloway, M. Hüther, D. Jaroszynski, L. Jensen, S. Jolly, A. Joulaei, M. Kasim, F. Keeble, Y. Li, S. Liu, N. Lopes, K.V. Lotov, S. Mandry, R. Martorelli, M. Martyanov, S. Mazzoni, O. Mete, V.A. Minakov, J. Mitchell, J. Moody, P. Muggli, Z. Najmudin, P. Norreys, E. Öz, A. Pardons, K. Pepitone, A. Petrenko, G. Plyushchev, A. Pukhov, K. Rieger, H. Ruhl, F. Salveter, N. Savard, J. Schmidt, A. Seryi, E. Shaposhnikova, Z.M. Sheng, P. Sherwood, L. Silva, L. Soby, A.P. Sosedkin, R.I. Spitsyn, R. Trines, P.V. Tuev, M. Turner, V. Verzilov, J. Vieira, H. Vincke, Y. Wei, C.P. Welsch, M. Wing, G. Xia and H. Zhang. *AWAKE, the advanced proton driven plasma wakefield acceleration experiment at CERN.* Nucl. Instrum. Methods Phys. Res. A **829**, 76–82 (2016).

72. A. Aschikhin, C. Behrens, S. Bohlen, J. Dale, N. Delbos, L. di Lucchio, E. Elsen, J.-H. Erbe, M. Felber, B. Foster, L. Goldberg, J. Grebenyuk, J.-N. Gruse, B. Hidding, Zhanghu Hu, S. Karstensen, A. Knetsch, O. Kononenko, V. Libov, K. Ludwig, A.R. Maier, A. Martinez de la Ossa, T. Mehrling, C.A.J. Palmer, F. Pannek, L. Schaper, H. Schlarb, B. Schmidt, S. Schreiber, J.-P. Schwinkendorf, H. Steel, M. Streeter, G. Tauscher, V. Wacker, S. Weichert, S. Wunderlich, J. Zemella and J. Osterhoff. *The FLASHForward facility at DESY.* Nucl. Instrum. Methods Phys. Res. At **806**, 175–183 (2016).

73. C. Joshi, E. Adli, W. An, C. E. Clayton, S. Corde, S. Gessner, M. J. Hogan, M. Litos, W. Lu, K. A. Marsh, W. B. Mori, N. Vafaei-Najafabadi, B. O'shea, X. Xu, G. White and V. Yakimenko. *Plasma wakefield acceleration experiments at FACET II.* Plasma Phys. Control. Fusion **60**, 034001 (2018).

74. A. Pukhov, Z. M. Sheng and J. Meyer-ter-Vehn. *Particle acceleration in relativistic laser channels.* Phys. Plasmas **6**, 2847–2854 (1999).

75. J. L. Shaw, N. Lemos, L. D. Amorim, N. Vafaei-Najafabadi, K. A. Marsh, F. S. Tsung, W. B. Mori and C. Joshi. *Role of direct laser acceleration of electrons in a laser wakefield accelerator with ionization injection.* Phys. Rev. Lett. **118**, 064801 (2017).

76. J. Ferri, X. Davoine, S. Fourmaux, J. C. Kieffer, S. Corde, K. T. Phuoc and A. Lifschitz. *Effect of experimental laser imperfections on laser wakefield acceleration and betatron source.* Sci. Rep. **6**, 27846 (2016).

77. C. F. Dong, T. Z. Zhao, K. Behm, P. G. Cummings, J. Nees, A. Maksimchuk, V. Yanovsky, K. Krushelnick and A. G. R. Thomas. *High flux femtosecond X-ray emission from the electron-hose instability in laser wakefield accelerators.* Phys. Rev. Accel. Beams **21**, 041303 (2018).

Printed by Media-Tryck, Lund 2019 NORDIC SWAN ECOLABEL 3041 0903

LUND UNIVERSITY
Faculty of Engineering, LTH
Department of Physics
Division of Atomic Physics

ISBN 978-91-7895-127-7 (print)
ISBN 978-91-7895-128-4 (pdf)
ISSN: 0281-2762
Lund Reports on Atomic Physics, LRAP 559 (2019)